Космични изследвания в България

Том 3 · София · 1980

Българска академия на науките

Address

Space Research in Bulgaria
Central Laboratory for Space Research
Bulgaria, 1000 Sofia, 1 Rouski Blvd.

Адрес

Космични изследвания в България
Централна лаборатория по космични изследвания
1000 София, бул. „Руски“ № 1

629.13(05)

Издателство на Българската академия на науките

Редактор *Н. Чакалова* Коректор *Ж. Тумпарова* Техн. редактор *Д. Калинова* 9532422211
Изд. индекс 7743 Дадена за набор на 30. VII. 1980 г. Подп. за печат на 6. XI. 1980 г. Код 28 2332-5-80
70×1000/16 Тираж 500 Печ. коли 4,13 Изд. коли 5,35 УИК 5,75 Цена 0,97 л
Печатница на БАН — 1113 София, ул. „Акад. Георги Бончев“ Пор. 418

Space Research in Bulgaria

Volume 3 · Sofia · 1980

Bulgarian Academy of Sciences

Contents

Содержание

BULGARIAN ACADEMY OF SCIENCES

SPACE RESEARCH IN BULGARIA, 3

Sofia · 1980

Development of Information Possibilities of Scientific Satellite Experiments

K. B. Serafimov, S. K. Chapkunov, T. N. Ivanova, I. B. Ivanov

A determinant factor in the contemporary stage of space research is the rapid increase of the information flux necessary to be transmitted to ground-based receiving stations. That is why special attention is paid to the information capacity increase in complex experiments, preserving the information capacities of the service satellite systems. This refers mainly to experiments involving studies of the structural parameters such as space plasma, solar wind and planetary atmosphere.

The problem of increasing the information possibilities in satellite experiments could be considered in two aspects, namely:

— The necessity to compress the information taken by the satellite, aiming at the decrease in the number of telemetric channels used. In this manner the possibility is created of performing new experiments and of using classical equipment for new additional measurements.

— The necessity, when a definite type of telemetric system is available (with limited information capacity), to establish conditions for recording data in special time intervals. This is the so-called intermediate information storage.

In the case of information compression the data are transformed so that, with quality preserved, the energy or the frequency band during emission is decreased, or the memory volume in data storage is reduced. The "shrink" effect cannot be determined simply as it depends exclusively on the methods of primary data presentation. Usually, with a given source whose limits are known in advance, this effect is evaluated by the degree of approximation to a minimum admissible volume to secure the informative capacity of its data.

There are three methods of information compression which are used more frequently. The first one is based on statistical coding and is subject to the theory of information. In this case the discrete data obtained through the phenomenon recorded are presented with the help of a definite number of symbols. During the statistical processing the volume of data stored is decreased, as the quantities which do not contain information for a given parameter are reduced.

The second method of compression is known as the interpolation and extrapolation method. Its effectivity does not differ from the first one, but it is easier to perform and can be applied successfully in cases when the parame-

ters of the source are not fully known. This method usually involves partial approximation of the initial characteristics to a known simpler function. Afterwards, instead of the entire characteristics, only the parameters specifying each sector of the approximating curve are transmitted [1].

The third method is applied usually in statistical measurements. In this case the experimenter is interested not in the momentum quantities of the parameter observed but in its mean value, dispersion, derivatives, etc. The replacement of the initial parametric totality by some of its characteristics is designated as parametric separation. This results in rapid volume reduction of transmitted or stored data. Typical of this method is the performance of inconvertible initial data transformations. So there are some doubts as to whether it can be taken as a compression method. It is clear that the final result makes it possible to relate this method to the one described above, notwithstanding the fact of the qualitative transition to a new data totality [2, 3, 4]. This method might require verification of the agreement between the data obtained during the experiment and the mathematical model of the phenomenon. It is a problem solved basically by statistical methods in the ground-based receiving stations.

In addition to the above methods there are others which, through one designation or another, could be related to the types already listed but which possess their own specificities.

By way of example we shall consider the information compression in probe methods of plasma diagnostics. These methods are used in studying the voltage-current dependence of conductor (probe) immersed into the space plasma. Usually a linearly changing voltage is applied to the electrode immersed in the plasma, and measurements are taken of the probe current of the input of a DC amplifier connected with the electrode (collector). The sawtooth sweep and the current signal amplified and transformed into voltage are recorded simultaneously. It is obvious that in order to transmit the volt-ampere characteristic thus obtained we need telemetry with sufficiently big capacity. This restricts the experiments performed on the same carrier and is not admissible, taking into account the fact that the probe measurements are usually accessory. In this case, the use of the equipment described in [3] to determine the probe characteristic derivatives reduces many times the volume of the information transmitted. The method described in [3] and the equipment initially used onboard the Ariel-1 satellite are interesting from the point of view of the possibilities provided for fully utilizing the Langmuir probe specificities. Measurements might be taken in this case of the thermal ion densities and temperatures (ion trap) or of the electron densities and temperatures (electron probe) in the ionosphere.

In the equipment considered use is made of the fact that the information necessary for the volt-ampere characteristics occurs in a more suitable and reasonable form if one deals with the curve derivatives.

The expression for the curve sector related to electron retarding can be presented as follows:

$$i_e = i_{e0} \exp\left\{\frac{eU}{kT_e}\right\} - i_+ - i_p,$$

where U is the probe potential (negative) with respect to the space potential; and i_+ and i_p are the positive ion current and the photocurrent, respectively. As U is negative, the i_+ and i_p currents change with the change of U much less than the current i_e. Then we obtain after differentiation by U

$$i'_e = \frac{e}{kT_e} i_e - \frac{ai_+}{aU} - \frac{ai_p}{aU} \approx \frac{e}{kT} i_e,$$

as well as

$$i''_e \approx \left(\frac{e}{kT_e}\right)^2 i_e,$$

therefore

$$\frac{i'_e}{i''_e} = \frac{kT_e}{e}.$$

For the linear part of the semilogarithmic characteristic this ratio is constant and its transmission by the telemetric system requires much smaller dynamic range than is the case when the curve itself is transmitted. Besides the electron temperature we can obtain the electron density, as this value corresponds to the refraction point of the characteristic.

The circuit used to obtain the derivatives is shown on Fig. 1. In order to determine the slope and the curvature of the characteristic, two voltages with small amplitudes are amplified and mixed. If the AC voltages are presented in the form of $U_1 \cos(\omega_1 t + \varepsilon_1)$ and $C_2 \cos(\omega_2 t + \varepsilon_2)$, where $\omega_1 \ll \omega_2$, then the expression for the current i could be written in the form of a row

$$i = i_e + i'_e[U_1 \cos(\omega_1 t + \varepsilon_1) + U_2 \cos(\omega_2 t + \varepsilon_2)]$$
$$+ i''_e[U_1 \cos(\omega_1 t + \varepsilon_1) + U_2 \cos(\omega_2 t + \varepsilon_2)]^2 + \cdots,$$

where the currents and their derivatives relate to values corresponding to the DC voltage value along the sweep at the moment t.

In this way the amplitude of the component with angular frequency $\omega_2(U_2 i'_e)$ yields the value of i'_e. In the circuit an automatic adjustment of gain is employed to keep constant the output signal of the first amplifier. The value i'_e which changes within broad limits is determined by the voltage of the automatic adjustment circuit. The quadratic term in the expression contains the component

$$2U_1 U_2 \cos(\omega_1 t + \varepsilon_1) \cos(\omega_2 t + \varepsilon_2)\, i''_e.$$

Therefore, the second output signal gives the modulation relative depth which is proportional to $2U_1 i''_e$.

The circuit shown in Fig. 1 differs from the one used in Ariel-1.

The reasons for making the given circuit complicated lie in the inconvenience of the suggested method. Actually, the above reasoning assumes that any deviation of the current carriers from the Maxwellian distribution would occur in instability of the ratio i'_e/i''_e and could be identified. In the general case, this is not observed even at net electron measurements where a sharp carrier potential change (in transition from light to nonlight orbital sector and the reverse, when other items of probe equipment are operating on the same carrier-satellite) could result in operation out of the linear-logarithmic region of the volt-ampere characteristic.

On the other hand, any occurrence of a new type of positive ions is reflected in a new slope of the volt-ampere characteristic for the ion measurements. This makes it still more difficult to decode the type of the characteristic derivatives. In general, the unavailability of the authentic volt-ampere characteristic is an essential defect which constitutes a specific feature of the third type of methods for information compression.

To a certain extent the reliability of the method [4, 5] could be increased by telemetry through given sufficiently long time intervals and the authentic volt-ampere characteristic. Furthermore, as shown on Fig. 1, it is possible to use the same number of telemetric channels. The full equipment description for Fig. 1 is given in [6].

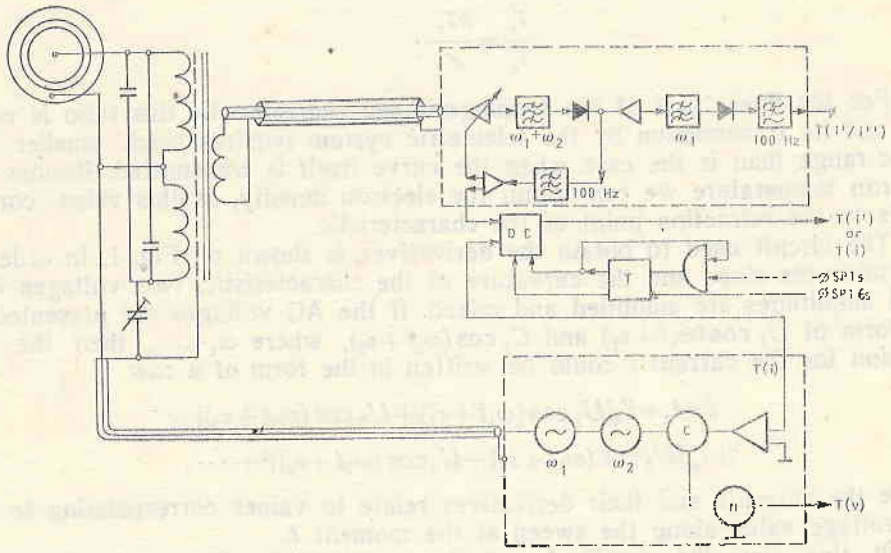

Fig. 1. Circuit diagram: DC — diode commutator, T — trigger, SP 1s and SP 16s — synchropulses, C — converter

Everything said until now refers to the first aspect of the problem of information possibility increase in satellite experiments.

If we continue developing the case presented in Fig. 1, we shall notice that all observations relate to direct data transmission regime, when the telemetric system information possibilities are sufficiently large. When we pass to data memory regime, basic for most of the satellite experiments, the number of points transmitted per time unit from the characteristics of interest decreases rapidly.

In probe experiments the interpretation is impossible in the case of a small number of points (e. g. under 12). That is why experimenters reach a compromise solution — decrease of the number of characteristics used at the expense of an increase of the number of points transmitted from a separate characteristic. This is the second aspect of the problem of information possibility increase, as mentioned in the initial part of this paper, namely, the establishment of record conditions in determined time intervals of interpretable data. The other denomination of this method is intemediate information storage.

The method consists of the following [7]: Over a certain period of time discrete measurements are performed with relatively large frequency of discretization, after which values obtained in the discrete measurements are transmitted over a period of time several times longer than the measurement period. Thus we obtain a picture of the measured volt-ampere characteristic,

stretched in time for establishing, under the above conditions, in order to increase the number of points transmitted at the expense of the number of characteristics taken down.

The block circuitry of such a memory device designed on the basis of the intermediate memory method is shown on Fig. 2. For considerations of con-

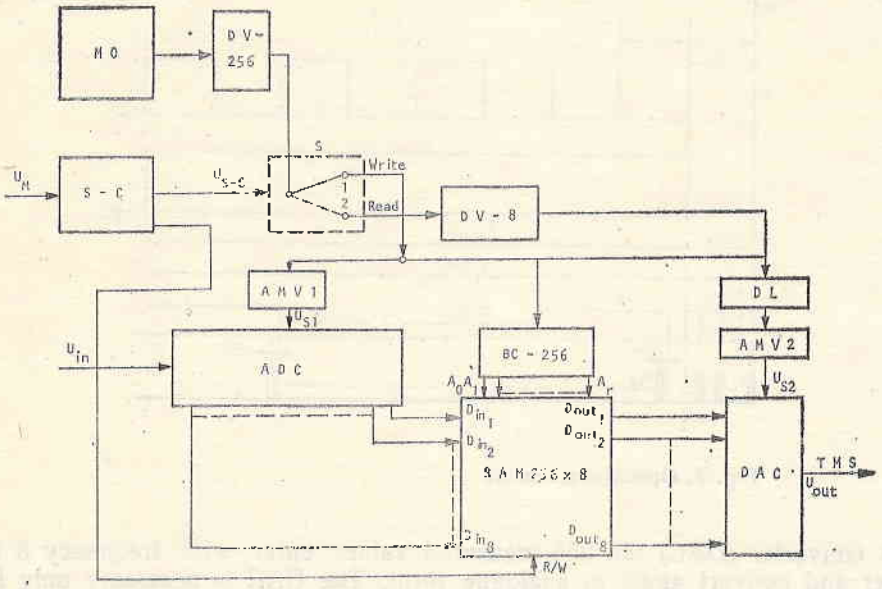

Fig. 2. Block-diagram of the memory unit: MO — master oscillator, S — electron switch, S-C — synchronizer-converter, ADC — A-D converter, BC-256 — binary counter, DV-8 and DV-256 — dividers, AMV 1,2 — multivibrators, DAC — D-A converter, RAM — real access memory

venience the operation is described based on a concrete circuit version. The master oscillator (MO) with square angle oscillation frequency of 65,563 kHz feeds the electron switch (S) through the divider (DV-256) with square voltage frequency of 256 Hz. The switch S is maintained by a synchronizer-convertor (S-C) [3] at the input of which a synchronizing voltage "meander" type U_M enters with a 2 s period of repetition (Fig. 3a). At the output of the S-C we obtain voltage U_{S-C} as shown on Fig. 3b. Therefore the record time T_{write} (1 sec in this case) of the controlling input of the switch S has a logical "0" and the reading time T_{read} (8 s in this case) has a logical "1". In the time interval "record" 256 strobes are fed V_{S1} (Fig. 3d) through the astable multivibrator AMV 1 to the A-D converter (ADC), i. e. at the rate of 256 measurements per second. At the same time, through the binary counter, up to 256 (BC-256) RAM memory addresses with organization 256×8 (Fig. 3c) are involved. As in the concrete case use is made of RAM type 1101a with access time of about 1 s, there immediately follows a transformation time requirement of ADC 1 s. As seen from Fig. 2, the A-D converter is of 8 bits with parallel output which feeds the memory. The control voltage from S-C feeds the bus READ/WRITE (R/W) as during the record there is a logical "1" at the input R/W and a logical "0" during reading.

The recorded information is transmitted after the measurement (T_{read}). The switch S is in position 2. The frequency divider DV-8 reduces 8 times the

frequency of the memory addresses involvement. The delay line DL is necessary to shift the strobes U_{S2} (Fig. 3d) from the astable multivibrator AMV_2 to 2 s with respect to the pulses controlling the addressing counter BC-256 (3c). This necessity arises from the time of memory access. So at the input of the

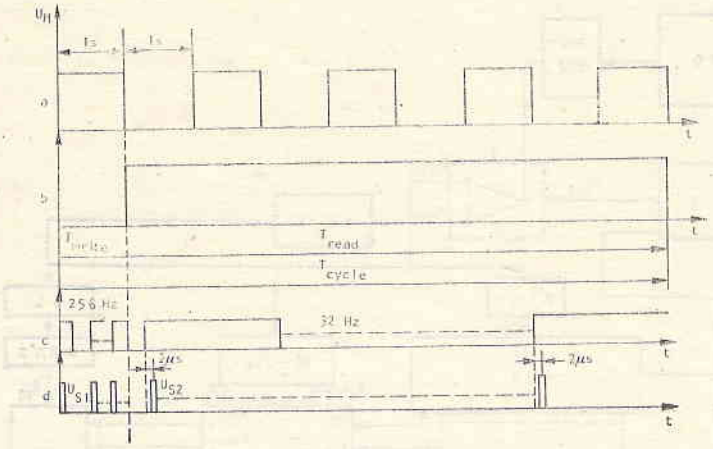

Fig. 3. Operations scheme

D-A converter (DAC) the 256 measured values enter with frequency 8 times lower and convert again in analogue form. The DAC is necessary only if the telemetric channels by which the information is transmitted are in an analogue form. In case they are digitals the DAC drops out of the circuit.

As the suggested intermediate memory device is used in different probe experiments with different types of volt-ampere characteristics, it is very difficult to determine simply according to Kotelnikov's theorem the necessary number of discrete measurements. That is why, on the basis of the structure shown in Fig. 2, it is possible to use storages of different capacities, as the frequency of the master oscillator and the capacity of the addressing counter would be subject to change.

Besides that, in the availability of digital telemetric channels, it is possible to use several telemetric channels simultaneously, especially in data transmission, with a certain complication of this structure. When we dispose of a microprocessor with an appropriately given programme (e. g. by first or second derivative change) the possibility arises of processing the volt-ampere characteristic recorded in the memory and of transmitting information only for special points from it.

Conclusion

The devices discussed above have been developed at the Central Laboratory for Space Research of the Bulgarian Academy of Sciences. Notwithstanding the fact that they are intended for probe measurements, the principles involved in their design could be employed in any type of space research where the final result is an analogue signal (volt-ampere characteristic). The reasonable employment of the possibilities of increasing the effectivity of space experi-

ments would lead to the full use of the experimental technique and equipment and of the satellite system. This could open up an entirely new stage in this field, particularly in routine space morphological measurements.

References

1. Ходарев, Ю. К., Б. Н. Родионов. Аппаратура для космических исследований. М. 1972.
2. Крамер, Г. Математические методы в статистике. — ИЛ, 1948.
3. Методы исследования плазмы. Под ред. В. Лохте-Холтгревена. М., 1971.
4. Bowen, P. J., R. L. F. Boyd, C. L. Henderson, A. P. Willmore. — Proc. Roy Soc., A. 281, 1964, 5. 526.
5. Wrenn, G. L. The Langmuir Plate and Spherical Ion Probe Experiments Aboard Explorer XXXI. — PIEEE, 57, 1969, 1072—1077.
6. Chapkunov, S. K. Scentific Probe Experiment with Preliminary Signal Processing. — In 3rd Conference of VMEI. Varna, 1975.
7. Chapkunov, S. K., I. B. Ivanov. — C. R. Acad. bulg. sci., 30, 1, 1977, p. 49.
8. Иванов, И. Б. Импулсен формировател. — Радио и телевизия, № 6,1978.

Повышение информационных возможностей научных спутниковых экспериментов

К. Б. Серафимов, С. К. Чапкынов, Т. Н. Иванова, И. Б. Иванов

(Резюме)

На современном этапе исследования космоса изучаются связи между явлениями, установленными прежними измерениями, и закономерностями в околоземном космическом пространстве. Это требует осуществления комплексных научных экспериментов. Резко возрастает поток научной информации, которая передается на наземные приемные станции. На этом этапе приходится решать вопросы, связанные с уплотнением информационных каналов; с сжатием передаваемого информационного потока, когда это возможно и целесообразно, иными словами — с повышением информационных возможностей научных спутниковых экспериментов. Коротко рассмотрены некоторые методы сжатия информации. Анализируется эффективность предварительной обработки информации. В качестве примера рассмотрен частный случай — космический зондовый научный эксперимент. Рассматриваются некоторые зондовые системы с предварительной обработкой сигнала и их информационные возможности.

BULGARIAN ACADEMY OF SCIENCES
SPACE RESEARCH IN BULGARIA, 3
Sofia. 1980

On the Possibilities of Digital Method Applications in Probe Space Experiments

S. Chapkunov, V. Genov, V. Markov

Recently the digital methods of information transmission find greater application in radiotelemetry, replacing the analog ones. That is due to the successful development of the pulse-digital technique and to some advantages of the digital systems compared to analog ones. The information signals from the ionospheric scientific experiments are analog in their majority. In order to be transmitted by the digital telemetric channels, it is necessary for the dynamic range of the analog process to be divided into a finite number of subregions, i. e. to be quantized by level. When the value of the measured quantity falls in some of the subregions, a value approximated to the closest higher or lowest level value is transmitted. If instead of this approximated value the number of the subregions is transmitted, then this method of transmission is called digital. A reestablishment of the quantized instantaneous signal value is performed in the receiving part through various methods of interpolation. The basic advantages of the digital methods, justifying them as a real and promising way to transmit information are: possibility of increase without informational losses, easy transfer and storage by one memory device into another, direct introduction into a digital computer, and possibility to increase the noise resistance of the system while introducing coding of informational excess.

The objective of this work is to evaluate the application possibilities of the principal digital methods in analog-digital informational transmission from direct probe space experiments.

We discuss and compare methods for: (a) pulse-code presentation with uniform quantization; (b) relative (difference) presentation; (c) delta-presentation.

Two determined probe signals are processed under linear and step interpolation.

We should note that the paper deliberately avoids the analysis of the adaptive informational presentation methods. The reason being: the relative complexity of equipment in the receiving and emitting part when using these methods; the variety and the relatively great possibilities of these methods is

subject to a separate analysis which could be further developed in another work.

The first analysed signal is the classical volt-ampere charactetistic of the Langmuir probe. The curve in Fig. 1 is a typical characteristic obtained dur-

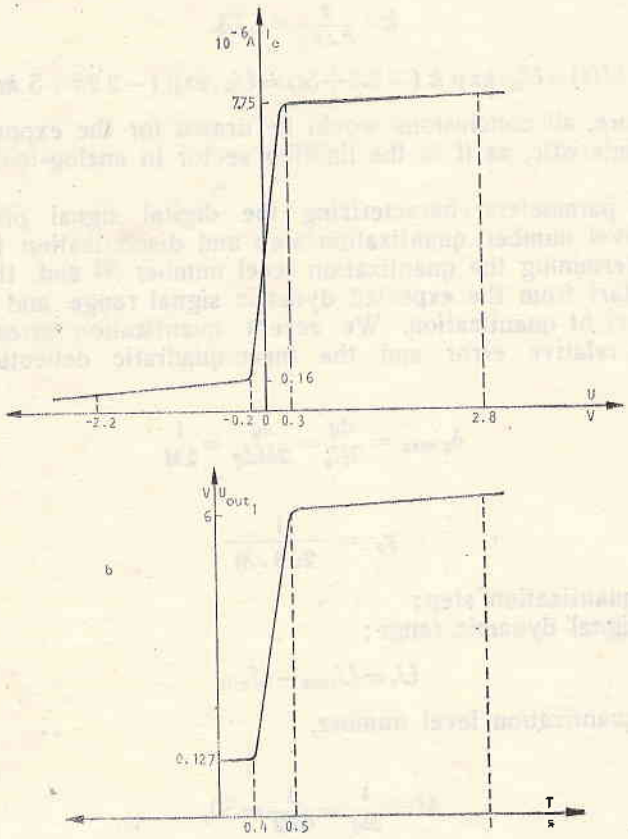

Fig. 1
a — Typical characteristics obtained during the operation of the Bulgarian probe equipment mounted onboard the Vertical-6 rocket (1977); *b* — The transformed characteristics of Fig. 1a

ing the operation of the Bulgarian probe equipment onboard the Vertical-6 rocket (1977).

Figure 1b shows the transformed characteristic of Fig. 1a taking into account that the sweep is linear and with period of 1 s.

The analysis and conclusions from the characteristic shown are valuable for the digital transmission of volt-ampere characteristics in general.

The minimal and maximal electron probe currents are, respectively, $I_{e\,min}=0.16\times10^{-6}$ A and $I_{e\,max}=7.75\times10^{-6}$ A. The maximal input level of the telemetric system $U_{in\,max}=6$ V and the minimal $U_{in\,min}=U_0=I_{e\,min}\cdot\frac{U_{in}}{I_{e\,max}}$ $=0.127$ V. The sweep voltage at values shown in Fig. 1*a* would be described by the expression $V_{sw}=-2.2+5t$ (t changing from 0 to T), and the exponen-

tial sector of the V-A characteristic can be presented analytically by the expression

(1) $$U(t) = U_0 . \exp\left(\frac{eU_{sw}}{k . T_e}\right) = U_0 . e^{k . U_{sw}},$$

where $$k = \frac{e}{k . T_e} = 7.73.$$

(2) $$U(t) = U_0 . \exp k\,(-2.2 + 5t) = U_0 . \exp\,(-2.2k + 5\,kt).$$

Furthermore, all conclusions would be drawn for the exponential part of the V-A characteristic, as it is the limiting sector in analog-to-digital transformations.

The main parameters characterizing the digital signal presentation are: quantization level number, quantization step and discretization frequency.

When determining the quantization level number M and the quantization step dk, we start from the expected dynamic signal range and the necessary accuracy (error) of quantization. We accept quantization error = 1 per cent. The maximum relative error and the mean-quadratic deflection are, respectively

(3) $$\delta_{q\,max} = \frac{dq}{2U_s} = \frac{dq}{2Mdq} = \frac{1}{2M}$$

and

(4) $$\gamma_q = \frac{1}{2\sqrt{3} . M},$$

where dq — quantization step;
U_s — signal dynamic range;

$$U_s = U_{max} - U_{min}$$

M — quantization level number,
hence

(5) $$M = \frac{1}{2\delta q} = \frac{1}{0.02} = 50,$$

but $M = 2^m$, therefore we chose the closest multiple to the 2^m number — $M = 64$. At 64 levels the mean-quadratic error from quantization would be $\gamma q = 0.46$ per cent.

The quantization step is equal to

(6) $$dq = \frac{U_s}{M} = 95 \times 10^{-8}\,\text{V}.$$

At uniform quantization, the quantization level is placed in the middle of the quantization interval. The absolute error obtained in identifying the instantaneous value with the quantization level is

(7) $$\varepsilon_q = \lambda_q - \lambda,$$

λ_q — quantization level;
λ — counted instantaneous value.
And the maximal absolute quantization error would be

(8) $$|\varepsilon_q|_{max} = \frac{dq}{2}.$$

The discretization frequency of the signal described in (2) is determined by its correlative function. This frequency should be within the limits 1.5 to 6 of the discretization frequency defined by Kotelnikov's theorem

$$F_0 = (1.5 \div 6) 2 \Delta f_{eff}. \tag{9}$$

The amplitude-frequency spectrum width is obtained from the spectra[1] density, calculated from the formulae in (1), in our case $\Delta f_{eff} = 30$ Hz.

We should underline that the discretization frequency can be determined more accurately by the relationship between the interpretation error and the signal correlative function.

When interpolating the examined signal with a polynomial of first power (step function), we obtain:

discretization period $T_0 = 0.004$ s,

discretization frequency $F_0 = 250$ Hz,

informational transmission rate $I = F_0 . m = 1{,}500$ bit/s.

At interpolation of the informational signal with the Lagrange polynomial of second power we obtain $T_0 = 0.0078$ s; $F_0 = 130$ Hz and $I = 780$ bit/s.

In differential methods of informational presentation the difference between two instantaneous values sampled in two subsequent discretization instants is quantized. These methods are valid only when there is a considerable decrease of the emitted informational quantity. It is obvious that the uniform difference representation could be valid when the signal fluctuates fast with small amplitudes and slowly changes within the limits of the full scale.

Therefore, the differential presentation is valid if an informational compression is obtained, i. e. if the difference between coordinates is encoded with less symbols than the discrete instantaneous value

$$m_d = m - \Delta m_d, \tag{10}$$

where m_d is symbols number in the difference coordinate,

m — symbols number with which the discrete instantaneous value is transmitted.

$\Delta m_d = E$ — where E is a full number minimal in the discretization range.

$$\Delta m_d = E \left\{ \frac{1}{2} \log_2 \frac{1}{2[1 - \hat{k}_l(T_0)]} \right\}, \tag{11}$$

where $\hat{k}_l(T_0)$ is the reduced signal correlative function.

For the case (Fig. 1b) we obtain $k_l(T_0) = 0.85$ at step function of interpolation and at the above-obtained values of T_0 and F_0. Hence $\Delta m = 0.85$ 1. Therefore, at difference presentation the number of binary symbols is the same one with which the instantaneous discrete value is given at pulse-code modulation with uniform quantization.

Upon linear interpolation and difference presentation we obtain $T_0 = 0.0078$ s; $\hat{k}_l(T_0) = 0.55$ and $\Delta m_d < 1$.

We see that the difference presentation of the symbol examined is not effective (at both ways of signal interpretation from Fig. 1), because of lack of information compression.

Upon delta-presentation of the signal the discretization frequency has to be selected in such a way that the function change per unit of discretization period would be less than the quantization step.

For interpolation with polynomial of first power, the quantization step is selected by the dependence

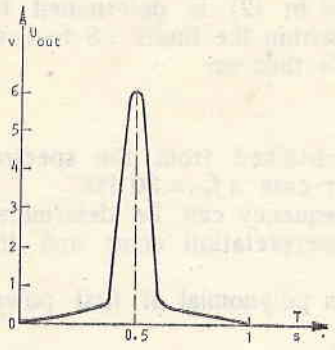

Fig. 2. A signal shape from an electron temperature study experiment with double modulation probe

$$\varepsilon_{max} \leq 2\,dq = 0.06\ \text{V},$$

$$dq \leq 0.03,$$

$$dq = 0.03\ \text{V},$$

for the discretization frequency we obtain

$$[U(t+T_0) - U(t)] \leq dq \quad F_0 = 1500\ \text{Hz},$$

for the interpolation with polynomial from second power

$$\varepsilon_{max} \leq dq = 0.06\ \text{V}$$

$$dq = 0.06\ \text{V}$$

$$F_0 = 720\ \text{Hz}.$$

The transmission rate of information quantity in both cases of interpolation is approximately equal to the rate in PCM, but this is achieved with much higher discretization frequency and the accuracy of this presentation method is much smaller because of the summing error effect from the different coordinates. For this signal type the classical PCM method appears to suit best in analog-digital presentation.

In many cases the information from V-A characteristic can be obtained with greater accuracy by their derivatives. Series of experiments prove that in practice [2, 3]. The signal shape from an electron temperature study experiment with double-modulation probe is shown in Fig. 2 and can be described analytically by the expression

$$U(t) = A \cdot \exp\left[-\frac{(t-t_m)^2}{2a^2}\right]$$

$$t_m = 0.5\ \text{s},$$

where

$A = 6\ \text{V}$ — signal amplitude,

$a = 30 \times 10^{-6}$ is determined by the condition $t - t_m = a$

$$U(a) = A \exp(0.5).$$

The processing results of this signal from the three digital methods with the described techniques are given in Table I.

As is seen from the Table, it is more reasonable for this signal also to use classical pulse-code presentation of the signal at linear interpolation. The relative presentation of this signal type has small coefficients of information compression (1.5) and upon delta-presentation in transmitting the same information much greater discretization frequency is necessary.

In conclusion, we can say that the digital methods application (namely, the classical pulse-code presentation) in probe methods is very effective when accompanied by prior processing of the V-A characteristic onboard the spacecraft. This processing should include the determination of the first and second signal derivatives. On the one hand, the differentiation decreases the dynamic range of the transmitted information, while on the other, it increases the ac-

Table 1

Type interpolation	Method of digital presentation	Level No. of quant. M	Quant. step d_k [v]	Discr. frequency [Hz]	Inf. trans. rate [bit/s]	Compr. coeff
Step interpolation	Classical pulse-code presentation	64	95×10^{-3}	110	660	—
	Relative (differ.) presentation	64	95×10^{-3}	100	500	1.5
	Delta-presentation	200	30×10^{-3}	2260	2260	—
Linear interpolation	Classical pulse-code presentation	64	95×10^{-3}	54	324	—
	Relative (differ.) presentation	64	95×10^{-3}	54	270	—
	Delta-presentation	200	60×10^{-3}	1670	1670	—

curacy of the measured parameters (electron density and temperature) and faciliates the ground-based computing of the telemetric information.

Such are in fact the development trends of the probe methods at the Central Laboratory for Space Research of the Bulgarian Academy of Sciences.

References

1. Мановцев, А. Р. Основы радиотелеметрии. М., 1973.
2. Tyler, A. F. The Radio and Electronic Eng., v. 42, No. 7, 1972.
3. Bowen, P. D., R. L. F. Boyd, C. L. Henderson, A. P. Willmore. Proc. Roy. Soc., A281, 526 (1964).

О возможностях применения цифровых методов в зондовых космических экспериментах

С. К. Чапкынов, В. Генов, В. Марков

(Резюме)

Рассмотрены возможности применения основных существующих методов аналого-цифрового преобразования для двух конкретных сигналов. В качестве конкретных примеров восприняты классическая вольтамперная характеристика, получаемая при применении зонда Ленгмюра, и характеристика,

получаемая при использовании двойного модуляционного зонда (для определения плазменной электронной температуры).

Частота дискретизации, число уровней и шаг квантования при заданной ошибке являлись основными параметрами для сравнения применимости различных цифровых методов.

Исследования двух конкретных примеров показали, что классическое код-импульсное представление обладает определенными преимуществами как по сравнению с разностным представлением (из-за отсутствия компрессии данных в последнем), так и по сравнению с дельта-представлением (из-за увеличения частоты дискретизации и ухудшения точности при дельта-представлении).

BULGARIAN ACADEMY OF SCIENCES

SPACE RESEARCH IN BULGARIA, 3

Sofia · 1980

Plasma Convection in the High-Latitude *F*-Region

R. A. Heelis

University of Texas at Dallas, Box 688, Richardson, Texas 75080, U. S. A.

Introduction

The convective motion of the *F*-region plasma at high latitudes is one of the most important parameters affecting its distribution and composition. Above invariant latitudes of about 60°, the dominant driving force for this convection is an electric field that originates outside the ionosphere. The electric field is produced in the magnetosphere, or at its boundary with the interplanetary medium, by an interaction between the geomagnetic field and the solar wind. The electric field is communicated to the ionosphere along the Earth's highly conducting magnetic field lines. Thus, our understanding of the high-latitude *F*-region plasma motion is not only necessary for a satisfactory description of the *F*-region itself, but can also contribute significantly to our understanding of the interaction of the Earth's atmosphere with the interplanetary medium. The existence of very different convection patterns is pointed out here, and their implications for *F*-region plasma distributions and for the interaction of the magnetosphere with the solar wind are discussed.

Observations

Measurements of the high-latitude ionospheric electric field have been made for several years on satellites [1] and balloons [2] using dipole antennas. Details of the electric field configuration on relatively small spatial scales are obtained from optical tracking of barium ion clouds [3]. More recently two and three dimensional *in situ* measurements of the *F*-region ion velocity have given more information on the nature of the global ionospheric motion [4, 5]. These measurements all agree that the dominant motion of the plasma above invariant latitudes of about 60° is one of two-cell-convection perpendicular to the magnetic field. Above invariant latitudes of 70° to 75° the plasma motion is generally directed away from the Sun with return flow toward the Sun at lower latitudes. The ion velocity is quite variable but is of the order of 1 km s^{-1} on the dayside and

500 m s^{-1} on the nightside. In the regions near dawn and dusk the boundary between sunward and antisunward convection may be well defined and has been termed "polar cap boundary" (the polar cap being the region of antisunward convection). While other definitions of the polar cap exist, this definition

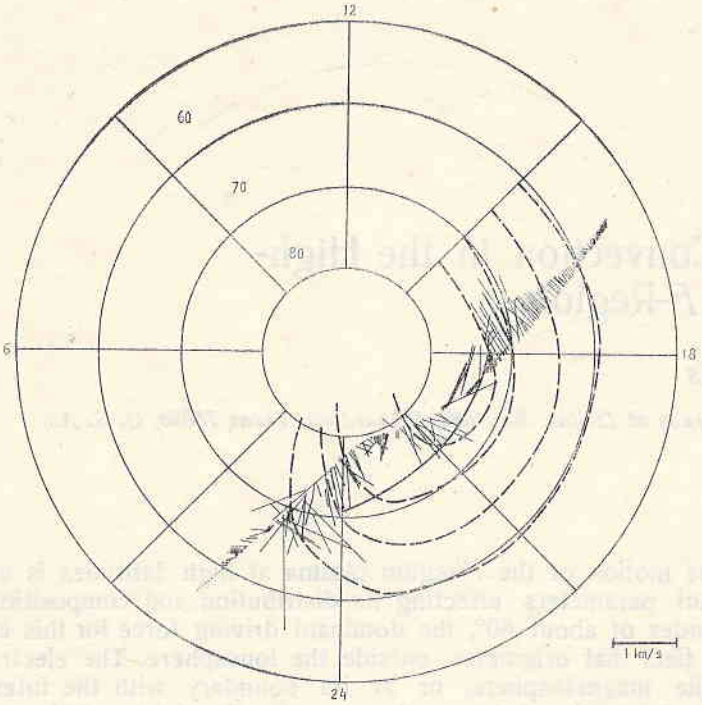

Fig. 1. Horizontal ion drift velocity vectors from AE-C orbit 13269. The dashed lines represent most probable convection trajectories drawn by eye. The heavy solid line is the location of the polar cap boundary which is assumed to be coincident with the poleward edge of the auroral zone

AE-C ; Ion drift velocities ; Day 76164 ; Orbit 13269 : Southern hemisphere
INVLAT V MLT

is used throughout this work. Near noon and midnight the flow changes from sunward to antisunward and vice versa, and the definition of the polar cap becomes less precise. Quite sophisticated theoretical models have been developed [6] to show that these generally observed features of the ionospheric convection pattern are consistent with an electric potential difference of between 50 and 100 kV applied across the magnetosphere. Simple convection models, assuming such a potential drop across the polar cap and assuming a centered magnetic dipole field with electric equipotential field lines, have been adopted for studying the *F*-region plasma distribution [7, 8]. Such studies have proved very illuminating and have made a positive step toward explaining some features of the high-latitude ionosphere. However, many features remain unexplained due to some severe restrictions imposed by the convection model. The most severe of these are probably that the convection inside the polar cap is directly antisunward and that the polar cap appears as a circle centered at the geomagnetic (geographic) pole.

Fig. 1 shows the horizontal ion drift velocity observed by the RPA/Drift Meter on the Atmosphere Explorer-C satellite [9, 10]. The data from the

southern hemisphere pass of orbit 13269 are shown on an invariant latitude (Λ) and magnetic local time (MLT) dial which is in a coordinate system co-rotating with the Earth. The lines extending from the spacecraft track are indicative of the direction and magnitude of the instantaneous ion velocity. The

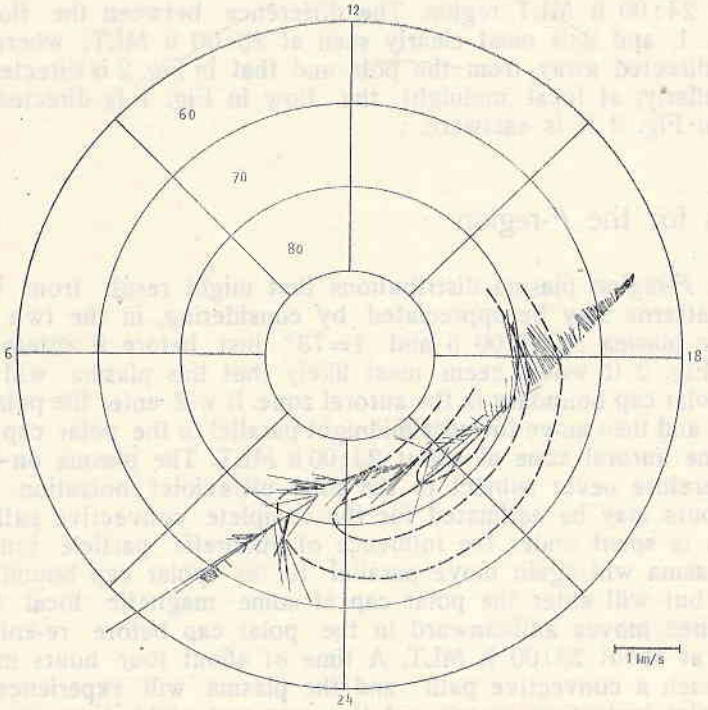

Fig. 2. Horizontal ion drift velocity vectors from AE-C orbit 13254: See Fig. 1 for details

AE-C; Ion drift velocities; Day 76163; Orbit 13254; Southern hemisphere INVLAT V MLT

scale is shown at the bottom right of Fig. 1. The dashed lines represent the most reasonable convective trajectories and have been drawn by eye with some attempt to conserve horizontal magnetic flux. While the data reveal one convective cell, it is not unreasonable to expect a second cell on the morning-side. The data are therefore consistent with the expected flow pattern. However, at about $\Lambda = 75°$ and 20:00 h MLT the flow inside the polar cap is not directed exactly antisunward, but rather it is directed away from the pole with a small component parallel to the noon-midnight plane and directed towards midnight. The arrow marks the boundary between flow components that are sunward and antisunward. It should also be noted that the noon-midnight meridian does not mark a line of symmetry in the convection pattern. This may be due to lack of symmetry altogether or to the fact that the line of symmetry has been rotated towards later local times.

Figure 2 shows the horizontal ion velocity vector observed by AE-C on the southern hemisphere pass of orbit 13254. While the location in invariant latitude and magnetic time is very similar to that shown in Fig. 1, the con-

vective signature represented by the dashed lines is very different. The variability of the observed ion velocity in the 20:00 to 21:00 h MLT sector is due to the passage of the satellite along the poleward edge of the auroral zone. This boundary is shown by the heavy solid line in Figs. 1 and 2, and is also representative of the polar cap boundary. These data are a dramatic example of flow in the polar cap which is not antisunward but eastward in most of the 18:00 to 24:00 h MLT region. The difference between the flow geometries in Figs. 1 and 2 is most clearly seen at 20:00 h MLT, where the flow in Fig. 1 is directed away from the pole and that in Fig. 2 is directed towards the pole. Similarly, at local midnight the flow in Fig. 1 is directed antisunward while in Fig. 2 it is eastward.

Implications for the *F*-region

The different *F*-region plasma distributions that might result from these two convection patterns may be appreciated by considering, in the two cases, the history of the plasma at 23:00 h and $\Lambda = 73°$ just before it enters the auroral zone. In Fig. 2 it would seem most likely that this plasma will move parallel to the polar cap boundary in the auroral zone. It will enter the polar cap near 19:00 h MLT and then move towards midnight parallel to the polar cap boundary. It re-enters the auroral zone at about 23:00 h MLT. The plasma on such a trajectory is therefore never subject to the solar ultraviolet ionization. A time of about two hours may be estimated for the complete convective path, at least half of which is spent under the influence of energetic particle ionization. In Fig. 1 the plasma will again move parallel to the polar cap boundary in the auroral zone but will enter the polar cap at some magnetic local time near 09:00 h. It then moves antisunward in the polar cap before re-entering the auroral zone at about 23:00 h MLT. A time of about four hours may be estimated for such a convective path and the plasma will experience both the solar ultra-violet ionization source and the casp and night time auroral zone particle sources. It should not be surprising that under identical auroral zone conditions over an order of magnitude, difference in observed total ion concentration may be expected at 23:00 h MLT just before the plasma enters the auroral zone. It has been assumed here that the ion velocity in the polar cap is uniform. There are even greater consequences to the *F*-region plasma distribution if the convection pattern of Fig. 2 represents a redistribution of the polar cap electric potential so that the plasma flows rapidly parallel to the polar cap boundary at the expense of very slow plasma flow in the middle of the polar cap. Then the plasma in Fig. 1 that convects through the dayside casp may reach $\Lambda = 80°$ at midnight about 1 h later. However, the same plasma flowing according to Fig. 2 may take many hours to reach the same location, leading to total ion concentrations that may differ by 2 or 3 orders of magnitude. Only the effect of the plasma convection on plasma in the polar cap has been discussed here. However, very subtle changes to the convection pattern can have dramatic consequences for the plasma distribution in the region of $\Lambda = 60°$. The symmetric centered convection model used in [7] and [8] predicts the existence of a flow stagnation point at 18:00 h MLT and about $\Lambda = 63°$. Unfortunately, such a location for the stagnation point cannot successfully explain the observed characteristics of the mid-latitude *F*-region trough. However, it has been shown [11] that a convection pattern similar to that in

Fig. 2 can move the stagnation point to magnetic local times as late as 23:00 h. Under these conditions theoretical models are in a position to reproduce many of the mid-latitude trough characteristics.

Implications for the Magnetosphere

The existence of field aligned currents and large field aligned potential differences [12, 13] makes the assumption that electric equipotential magnetic field lines extend from the ionosphere to the magnetosphere extremely dangerous. It would also suggest that the mapping of observed *F*-region electric potential distributions into the magnetosphere is of dubious value. However, if it is assumed that the flow configuration near the *F*-region polar cap boundary is at least qualitatively similar to the flow near the corresponding boundary in the magnetosphere, then the *F*-region observations may become extremely useful. Whether this corresponding boundary lies at the magnetopause or inside the magnetosphere depends on the nature of the interaction of the magnetosphere with the solar wind. The flow configuration of Fig. 1 suggests that there is a substantial flow across the polar cap boundary throughout the nightside. This may imply that in an open magnetosphere a region of reconnection extends across a substantial portion of the magnetotail. Alternatively, it may indicate that the "viscous interaction" associated with a close magnetosphere gradually weakens as the plasma moves down the tail. Figure 2 would suggest that in an open magnetosphere a region of reconnection in the tail occupies only a small region near local midnight and that all the antisunward convecting plasma converges towards this point under the influence of the solar wind electric field. Alternatively it may suggest that the degree of "viscous interaction" in a closed magnetosphere is very strong and that the boundary layer flow extends well down the tail. It should be pointed out that the existence of a boundary layer flow and an open magnetosphere are not mutually exclusive. The situations described here represent the classical extremes of open and closed magnetospheres.

A quantitative description of the *F*-region plasma distribution depends not only on the convective motion of the plasma but also on the details of the different sources and sinks of ionization that are encountered during the convective motion. It is therefore important to establish the relationship between particle precipitation zones and plasma convection patterns. While it has been shown that very different convection signatures can be observed, there is no evidence offered for the stability of these patterns on time scales of the few hours required for their completion. It may be confidently expected that the convection patterns depend on substorm activity and other solar and interplanetary magnetic parameters which change on time scales of 1 hour.

The construction of a model convection pattern which may represent the observed flow characteristics under given solar and magnetic conditions is of great importance to successful modelling of the high latitude *F*-region.

The understanding of high-latitude *F*-region convection will not shed light directly on the nature of the interaction between the magnetosphere and the solar wind. However, the behaviour of this convection and its relationship to the field aligned current distribution and energetic particle precipitation zones may help to assess the relevance of such data to magnetospheric processes. In particular, the behaviour of the *F*-region plasma flow near the polar cap boundary as a

function of substorm activity and changes in other solar and magnetic parameters may well be indicative of the variability of the magnetosphere-solar wind interaction. The needed *in situ* measurements of the magnetosphere and solar wind are, or soon will be, undertaken. Simultaneous measurements of electric fields, plasma motion, field aligned currents and energetic particles in the ionosphere will be undertaken by the Dynamics Explorer Satellites and by Intercosmos satellite payloads. The data from these satellites will prove valuable to the advance in understanding of the dynamics of the high-latitude ionosphere.

Acknowledgements. I would like to thank Dr. W. B. Hanson for stimulating my interest in this work and for giving me the opportunity to work with the AE data. The AE data analysis and presentation was supported by NASA under 034—3584.

This paper was prepared at the Central Laboratory for Space Research in Sofia during a visit supported by the National Science Fondation under grant 0213-543, and by the Bulgarian Academy of Sciences. I would like to thank Dr. F. S. Johnson at U.T.D. for giving me the opportunity to participate in the joint U.S.-Bulgarian exchange and to Dr. I. Kutiev, Prof. Dr. K. Serafimov and associates at the Central Laboratory for their hospitality during my stay.

References

1. Cauffman, D. P., D. A. Gurnett. — Space Sci. Rev., 13, 369, 1972.
2. Mozer, F. S., R. Serlin. — J. Geophys. Res., **74**, 4739, 1969.
3. Wesoott, E. M., J. D. Stolarik, J. P. Heppner. Particles and Fields in the Magnetosphere. D. Reidel, 1970, p. 229.
4. Galperin, Yu. I., V. N. Ponomarev. — Rep. 130 Acad. Sci. of USSR, Inst. for Space Res. Moscow, 1972.
5. Heelis, R. A., W. B. Hanson, J. L. Burch. — J. Geophys. Res., 81, 3803, 1, 1976.
6. Wolf, R. A. Magnetospheric Physics. D. Reidel, 1974, p. 167.
7. Knudsen, W. C. — J. Geophys. Res., 79, 1046, 1974.
8. Hanson, W. B., D. R. Zuccaro, C. R. Lippincott, S. Sanatani. — Radio Sci., 8, 333, 1973.
9. Hanson, W. B., R. A. Heelis. — Space Sci. Instrum., 1, 496, 1975.
10. Spiro, R. W., R. A. Heelis, W. B. Hanson. — J. Geophys. Res., 83, 1978.
11. Iijima, T., T. A. Potenra. — J. Geophys. Res., 81, 2165, 1976.
12. Swift, D. W. — J. Geophys. Res., 80, 2096, 1975.

Конвекция плазмы в высокоширотной *F*-области

Р. А. Хилис

(Резюме)

Измерения скорости ионов в высокоширотной F-области показывают, что конвекция может иметь довольно разную конфигурацию. При изменении конфигурации конвекции можно ожидать в данном месте разницы в ионной концентрации на несколько порядков. Эти изменения, вероятно, являются результатом разной степени взаимодействия между магнитосферой и солнечным ветром.

BULGARIAN ACADEMY OF SCIENCES

SPACE RESEARCH IN BULGARIA, 3

Sofia · 1980

Delta-Modulation Digital Processing of Videoinformation

D. N. Mishev, P. V. Petrov

The differential method of analog signal one-bit coding — the delta-modulation (DM) — is largely acknowledged as a means of economical digital coding in data transmission through a communication channel. The advantages and the shortcomings of the method in this respect are widely known [1, 2, 3]. Recently certain reliability consolidation of the delta-modulation as a method of informational coding has been noted [4] and first attempts at DM digital processing have been made [5, 6, 7, 8] but they were more of an incidental rather than systematic nature.

On the other hand, because of the lower rate of the DM binary digital stream compared to the normal or logarithmic PCM at adequately satisfiable quality of coding (referring to the signal-to-noise ratio SNR) and of the considerably simplified instrumental design compared to other coding methods (for instance DPCM), we may consider the DM method as particularly favourable for videoinformational digital processing.

The purpose of this paper is to present a systematic overview of the DM possibilities in digital processing in general and to consider some specific processing properties of this coding type. As far as the authors are informed, this may be a first approach of that kind.

1. Differential Calculations and Delta-Modulation

The differential algorithms with finite number and step size represent a significant portion of the contemporary digital methods applied with finite state machines (both in step and operational number).

While the differential calculus provides the principles, it can be shown that the DM is a natural basis for applying these principles in a general sense. For instance, we can find analogy between the differential algorithms of a uniform set and the synchronous DM or between the differential calculus of nonuniform interpolation sets and some specific types of asynchronous DM. The linear synchronous DM represents the input signal only by constant finite differences [1] although there are varieties (adaptive and/or asynchronous) [9, 10], where these differences are distinguished between themselves. The

inear DM does not represent the input signal itself through the finite differences of the 1st order but rather its linear interpolation (with splines of the 1st order, therefore the macrointerpolation, as far as they interpolate among themselves in certain cases, is of "zero" order), and the accuracy is provided on account of the increased clock frequency (i. e. increased number of interpolation blocks).

Let us consider a function of a variable determined over a discrete set of equidistant points, i. e.

$$\{f_k : f_k = f(x_0 + kh),\ h = \text{const}\}_{k \in M}, \tag{1.1}$$

$$x = \{x_k,\ x_k = x_0 + kh,\ h = \text{const}\}_{k \in M}, \tag{1.2}$$

$$M = \{m\ |m| \in N_0\},\ N_0 = \{0, 1, 2, \dots\}, \tag{1.3}$$

where M is the index set of the interpolation set. The differential operator can be determined [11] as

$$\Delta f(x_i) = f(x_i + h) - f(x_i) = f_{i+1} - f_i. \tag{1.4}$$

The differential operator contribution to the various arithmetic processes is of particular importance to the further examination of the relationship between the signal digital processing and the delta-modulation processing system. This operator is linear [1]. Its effect on products of two functions, for instance, can be represented by

$$y_i = \varphi_i \psi_i$$

$$\Delta y_i = \Delta[\varphi_i \psi_i] = \varphi_{i+1} \Delta\psi_i + \psi_i \Delta\varphi_i = \varphi_i \Delta\psi_i + \psi_i \Delta\varphi_i + \Delta\varphi_i \Delta\psi_i. \tag{1.5}$$

The operator for the n-th derivative can be represented as (1.6) [12, 13] based on the differential Table for uniform interpolation set and sufficiently differentiable function

$$\frac{d^n}{dx^n} = \left[\frac{1}{n} \ln(1 + \Delta y)\right]^n = \frac{1}{h^n}\left(\Delta y - \frac{1}{2}\Delta^2 y + \frac{1}{3}\Delta^3 y - \dots\right)^n \tag{1.6}$$

$$x_i \in X.$$

Then for the first derivative it yields

$$y_i' \approx \frac{1}{h} \Delta y_i \tag{1.7}$$

as approximation for functions with finite spectrum at sufficiently populated interpolation set or

$$\#M > A, \tag{1.8}$$

where $\#M$ is the cardinal number of the index set and A depends on the spectrum type, i. e. condition (1.8) is equivalent to sufficiently large clock-frequency in the DM processing system

$$f_c > f_a, \tag{1.9}$$

where f_c is the clock-frequency of the DM system.

There are other types of numerical differentiation [12], appropriate to the given case.

At functions of two arguments $z = f(x, y)$, which represent the natural generalization of different picture types, we can define by analogy (1.4) a linear differential operator [12, 14]. Referring to the latter, the interesting processing cases, e. g. (1.5), (1.7), can be generalized as well.

The prediction process in delta-modulation models another approximative curve with spline functions of the respective order, following the main process in the discretization points

$$\delta_\tau^k: \begin{cases} z_{i-1} = \operatorname{sign}(c_i - y_{i-1}), \ z_i \in \{-1, 1\} \\ y_i = y_{i-1} + z_{i-1}, \ k, \ k = \text{const}, \end{cases} \tag{1.10}$$

is valid for the linear DM, where δ_τ^k is the delta-transformation of the analog signal, $x(t)$ by the DM coder with k-step and duty cycle interval $\tau = \frac{1}{f_c}$; y_i is the approximated signal respective value $c_i = c(t_i)$ and z_i is the delta-modulator output jump, normalized to the step, prior to encoding into a binary code. The approximating process y_i can be represented as resulting from the two corresponding sequences of the differential table for y_i, and the specific feature of the Table is the fixed value of the first difference.

The differences available in the differential tables for the input signal and the approximation would result mainly from the distortions within the coding process, i. e. from the quantizing noise and from the slope overload noise. If we average within a given finite interval $T = n\tau$ by the dependence

$$\Delta y_m = y_{m+1} - y_m = k \sum_{i=(m-1)n+1}^{mn} z_i, \tag{1.11}$$

i. e. if we build up the first two columns of the differential table over the depopulated interpolation set $x_c^m - x_y^m$, where the dependence

$$\# x_c^m = \frac{\# x_c^i}{n} \tag{1.12}$$

is valid, then between the cardinal numbers of the index sets there is a certain approximation of the two tables in the case of optimal signal quantization $c(t)$ (with respect to the signal-to-noise ratio — SNR). Otherwise, the approximation differentiational table would appear in a rather tough form, compared to the input signal table.

By analogy, in other DM types there is an interrelation between the output sequence of the DM coder variations

$$z\delta_c = \{z_i\}_{i \in N} \tag{1.13}$$

and the differential table of the input signal, respectively.

2. Delta-Modulation Operations

If we satisfy the familiar requirements [15] for an optimal DM coder, we may consider x_i^q for an accurate digital representation of x_i^q by amplitude.

The delta-transformation of the input signal $c(t)$ can be represented as a binary sequence

$$\delta_c = \{B_i\}_{i \in N}, \ B \in \{0, 1\}, \tag{2.1}$$

where N is the index set.

If $f(t)$, $u(t)$ and $v(t)$ are the actual input signals, represented by time functions with a finite spectrum, and their DM transformations are $\delta(f)$, $\delta(u)$

and $\delta(v)$ and the operation $F_i^q = U_i^q * V_i^q$ is effected, the processing could be subdivided into three classes depending on the result type.

a) the output gives the finite differences, $\Delta F_i^q = F_{i+1}^q - F_i^q$ in digital form coded into the respective binary code.

In that case the process can be represented as an output of a differential coder with a pulse-code modulation (DPCM) which encodes the respective resulting signal, composed by the DM approximations of signals and $u(t)$ and $v(t)$

$$\Delta F_i^q = \varphi(\delta u, \delta v, *); \tag{2.2}$$

b) the output is represented in DM type $B_i^f = \psi(B_i^u, B_i^v *)$, where B_i^f, B_i^u, B_i^v are respectively the i-th binary symbols from the corresponding sequences, i. e.

$$\delta f = \psi(\delta u, \delta v, *); \tag{2.3}$$

c) the result is represented as a DM approximation F_i^q before or after LF-filtering, decoded respectively, i. e. both result processing and decoding are effected

$$F_i^q = \chi(\delta u, \delta v, *). \tag{2.4}$$

Both cases (a) and (b) permit uniquely the direct digital representation of the signal in the respective system code (by accumulation of F_i^q from (2.2) and (2.3)). Case (c) is valid when the transformation χ is invariant with respect to the binary sequences δu, δv or to their resultant and the operation $*$ is mostly realized by variations of the DM decoder parameters.

3. Spatial Invariant Transformations of Pictures

The picture $I = B(x, y)$ can always be represented through a screen scanning system as a function of one argument $B(t) = B[x(t), y(t)]$ through the evolved functions $f_x(t)$, $f_y(t)$ [16, 17, 18], where

$$U_I = U[B(t)] = U\{B[x(t), y(t)]\} \tag{3.1}$$

is the output signal of the screen system.

Let transformation $\delta_\tau^h(U_I)$ be effected by the DM decoder (1.10). It will transform the continuous signal of the evolving system $u(t)$ into the binary sequence δu

$$\delta_\tau^h : u(t) \to \delta u(i). \tag{3.2}$$

Therefore, the picture I is transformed into the sequence δu, through the composition of the screen system and the DM coder (Fig. 1). When decoding the δu by appropriate decoder $(\delta_\tau^{h'})^{-1}$ the signal $U'(t)$ could be obtained which corresponds to the picture I'. Thus the spatial invariant operations concerning contrast variations, inversion, peculiarity outlining, and quantization [20] can be readily effected.

We call spatial invariant operations those which accept translation i. e. when the operational composition over the picture φ and the translation $T_{a,b}$ are commutative [19].

If the operation φ is such that $\varphi[f(x, y)]$ depends uniquely on $f(x, y)$, i. e. there exists an $\chi(f)$ such that

$$\varphi[f(x, y)] = \chi[f(x, y)] = \chi(f_i), \ \forall f \in \varphi, \ \forall (x, y) \in S \tag{3.3}$$

is valid, where φ is the picture set within which the operation φ is realized in the definition region of S, then φ would be the by-element operation for the picture I. If χ is linear and of the type

$$\chi = \chi(f_i) = p \cdot f_i. \tag{3.4}$$

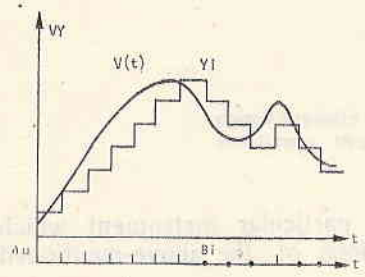

Fig. 1. Picture I is transformed into the sequence δu

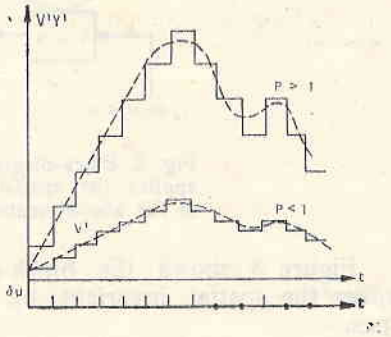

Fig. 2. Spatial invariant transformation of picture by the composition(3.5)

t could be easily effected by the composition between the direct and reverse DM transformations.

$$\delta_\tau^{k_1} \circ (\delta_\tau^{k_1})^{-1} \tag{3.5}$$

according to the scheme

$$I \xrightarrow{f_{xy}} U(f) \xrightarrow{\delta_\tau^{k_1}} \delta_u \xrightarrow{(\delta_\tau^{k_2})^{-1}} U'(f) \xrightarrow{f_{xy}^{-1}} I'. \tag{3.6}$$

The new signal $U'(t)$ amplitude will attain the value

$$A_1 = A_0 \frac{k_2}{k_1} = A_0 p. \tag{3.7}$$

Obviously picture I is transformed into I' (3.6), where $\varphi: I \to I'$ and $\varphi[f(x, y)] = \chi(f_i(x, y)) = kf_i$ as far as the picture I geometry is not deformed, φ is the spatial invariant and actually

$$\forall f \in \varphi,\ \forall (x, y) \in S,\ T_{a,b}[\varphi(f)] = T_{a,b}[kf_i] = kf_i(x-a, y-b) = k(T_{a,b}(f_i))$$
$$= \varphi[T_{a,b}(f)] \Rightarrow T_{a,b} \circ \varphi = \varphi \circ T_{a,b}. \tag{3.8}$$

Figure 2 shows the cases $p>1$, $p<1$. Under operation we understand precisely the composition (3.5), i. e. the realization of the linear by-element operations of the type χ by DM is adequate to the signal coding of the evolving system $U(t)$ by the point $\delta_\tau^{k_1}$ in the plane of the linear DM transformations and its reconstruction at point $\delta_\tau^{k_2}$ from the same plane [20].

$$\begin{array}{ccc} I & \xrightarrow{\varphi} & I' \\ \downarrow & & \uparrow \\ U(t) & \xrightarrow{\delta \circ \delta^{-1}} & U'(t) \end{array}$$

This type of processing is of the class (2.4) because the output DM sequence δu is invariant with respect to the operation. By analogy, there could be realized operations of contrasting over determined levels, outlining of specifics and others [20] by appropriate restrictions over φ of the by-element operations.

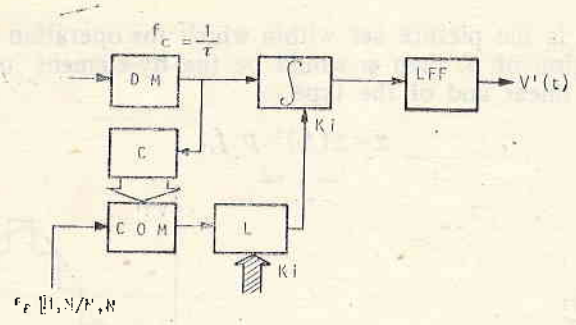

Fig. 3. Block-diagram of that particular element which applies the spatial invariant by element operations of the above-mentioned types

Figure 3 shows the block-scheme of that particular instrument which applies the spatial invariant by element operations of the above-mentioned types.

4. Scale Transformations*

A single representation of the signal $U(t)$ (3.2) is realized by the transformation δ_τ^k (3.2), which is invariant with respect to the scales of the two coordinates of the signal and to the coordinates of the picture itself, respectively, since it is adequately represented by the screen system. In contrast to (3.5), here the composition will be

$$\delta_{\tau_1}^k \circ (\delta_{\tau_2}^k)^{-1} \tag{4.1}$$

because the scale transformations over picture I are attached to it by $U(t)$ of the screen system. It is clear that all similar (purely scalar) operations will be represented in the plane of the DM transformations [21] by segments parallel to the abscissal axis $O\tau$. The dependence between the coded and decoded signal in that case will be

$$U'(t) = U\left(t\,\frac{\tau_2}{\tau_1}\right), \tag{4.2}$$

i. e. in fact we have "extension" ("compression") of $U(t)$ up to $U'(t)$ or the linear picture scale variation takes place because of deformation in the temporal axis in the screen system by φ, obviously the signal temporal deformations $U(t)$ evolve frequency deformations, according to the compression theorem of the Fourier transformation and the signal $S(\omega)$ spectrum becomes

$$\begin{array}{ccc} I & \xrightarrow{\varphi} & I' \\ \downarrow & & \uparrow \\ U(t) & \xrightarrow{\delta,\delta^{-1}} & U'(t) \end{array}$$

$$S'(\omega) = \frac{\tau_2}{\tau_1} S\left(\frac{\tau_1}{\tau_2}\,\omega\right), \tag{4.3}$$

i. e. the signal spectrum components $\{\omega_i\}_{i\in N}$ will transform into $\left\{\omega_i \frac{\tau_1}{\tau_2}\right\}_{i\in N}$, and the period of the transformed signal $U'(t) = U'\left(t + \frac{\tau_2}{\tau_1} T'\right)$ will be $T' = kT$.

* By scale transformations over I we understand here the transformations of the linear scale towards the rapid scanning of the screen system, for instance for the sweep f_x.

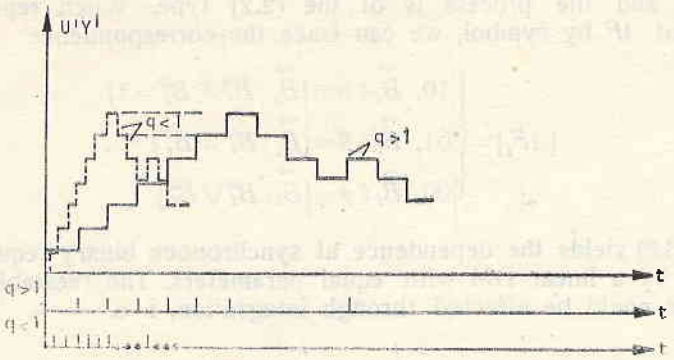

Fig. 4. Scale transformation

The new signal $U'(t)$ will be received at the DM decoder with the same SNR as in possible reconstruction of $U(t)$ in the same coding point of the $\delta^k_{\tau_1}$ signal, i. e. both direct and reverse DM transformations are equally optimal with respect to the SNR. Indeed, the familiar formula [1] for the SNR_{max} yields

$$SNR_{max} = \frac{c \cdot f_c^{3/2}}{f_0 \cdot f_m^{1/2}}, \tag{4.4}$$

where $f_c = 1/\tau$ is the DM clock frequency, f_m is the boundary frequency of the lowpass filter LPF permeability into the DM coder, and f_0 is the frequency of the processed harmonic signal, i. e. SNR is invariant with respect to the frequency region deformation equal for both the decoder and the signal.

Figure 4 shows the two possible cases of temporal scale changes of $U(t)$ at $q = \frac{\tau_2}{\tau_1} > 1$ "extension" and $q < 1$ "compression". Because of the screen system the picture would change geometrically along the same axis proportional to q or

$$\delta_{\tau_1} \circ \delta^{-1}_{\tau_2} [f(x, y)] = f(qx, y) = \varphi(f). \tag{4.5}$$

Operations of type (4.5) are intercommutant at certain conditions [21], which significantly facilitates repetitive processing.

5. Application of Some Arithmetic Operations

5.1. Addition

The operation can be represented as

$$F_l^q = U_l^q + V_l^q. \tag{5.1}$$

By analogy with the differential operator effect in the arithmetic operations point 1, [11] the addition in this case could be represented by $z\delta u$ and $z\delta v$

$$\Delta F_l = z_l^u + z_l^v. \tag{5.2}$$

It can be proved that

$$\Delta F_l \in \{-2, 0, 2\} \tag{5.3}$$

is valid [22] and the process is of the (2.2) type. When representing the DPCM output ΔF by symbol, we can trace the correspondence

$$(5.4)\qquad |\Delta F_i| = \begin{cases} 10, \ \vec{B}_i \in \alpha = \{\vec{B}_i \mid B_i^u \wedge B_i^v = 1\} \\ 01, \ \vec{B}_i \in \beta = \{\vec{B}_i \mid B_i^u + B_i^v\} \\ 00, \ \vec{B}_i \in \gamma = \{\vec{B}_i \mid B_i^u \vee B_i^v\} \end{cases}.$$

Expression (3.8) yields the dependence at synchronous binary sequences δu and δv obtained by a linear DM with equal parameters. The reestablishing of the actual values could be effected through integration, i. e.

$$(5.5)\qquad F_i = \sum_{j=0}^{i-1} \Delta F_j > \sum_{j=0}^{i-1} (z_j^u + z_j^v).$$

The logical scheme through which (5.2) is transformed into (5.4) is shown in Fig. 5 as the integration over (5.5) can be effected by reversive counter shown with dashed line (the amplitudinal recovery in the differential methods is reduced always to integration and therefore this counter is typical for any similar operation).

In general the addition of n-variables could be effected also by the corresponding DM transformations [22] and into the three possible types — (2.2), (2.3) and (2.4), respectively.

It can be shown that the subtraction reduces to logic inversion composition of one sequence and addition [22] (Fig. 6).

5.2. *Multiplication*

Let us assume necessary to perform operation

$$(5.6)\qquad F_i = U_i V_i.$$

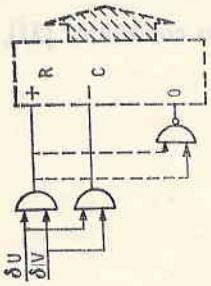

Fig. 5. Addition of 2-variables

If the differential operator affects this expression and the finite difference (1.5) is formed when replacing the corresponding differences with the DM jumps z_i^u and z_i^v, we can obtain

$$(5.7)\qquad \Delta F_i = z_i^v \sum_{j=0}^{i-1} z_j^u + z_i^u \sum_{j=0}^{i-1} z_j^v + z_i^u z_i^v$$

at the input signal. Expression (5.7) yields the digital jump when a product of the respective DM transformations δu and δv is formed with equal parameters ε and k. In integrating the differences we can obtain the product itself.

The adding procedure does not express clearly the advantages of any of the three representations of the output signal (2.2), (2.3) and (2.4). The multiplication procedure will yield a very complicated solving rule (5.7) at output of the (2.3) type [22], and the algorithmic noise of the operation will be significant. This noise can be distributed as additional into both categories of DM noise—from quantization N_Q and from slope overload N_s. The output realization

(2.4) is impossible because of changes in the invariance condition (point 2.c).A block-scheme of the (2.2) type is shown in Fig. 7.

The reversive counters RC U and RC V integrate the corresponding binary sequences δu and δv. The multipliers with values $N\times 1$ in fact determine only the

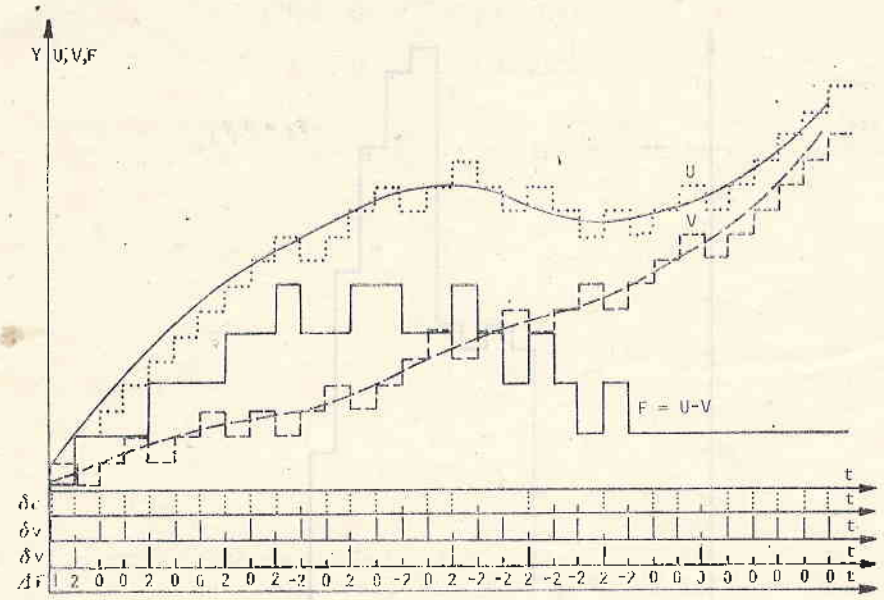

Fig. 6. Subtraction reduces to logic inversion composition of one sequence in addition

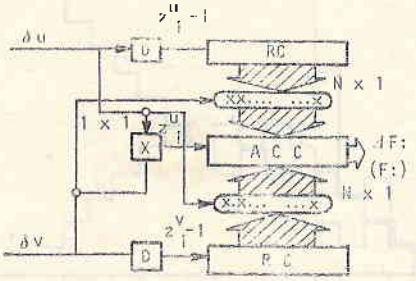

Fig. 7. Block-diagram of the multiplication, (2.2) type

sign of the result yielded by the counters when adding that to the accumulating adder. When the annulation of the accumulating adder is effected at each duty cycle, ΔF_i will be obtained at its output in the opposite case F_i could be accumulated in the same adder. The multiplier of value 1×1 determines the sign of the adder unit in the LSB order of the adder. Figure 8 shows the result approximations of the respective signals of the binary sequences and digital values of ΔF_i.

This technique could result in a great number of operations which are interesting for the videoprocessing of the spectrozonal scan videoinformation for the needs of the remote sensing. For instance, in a similar way we can

present the Riemann and Stilte's integrals [23] and some integral transformations as well. The contouring of some specific features could be effected also by this technique, once by the respective DM analogies to (1.7) [24] in different directions [25, 28, 27] and also when realizing some gradient operators

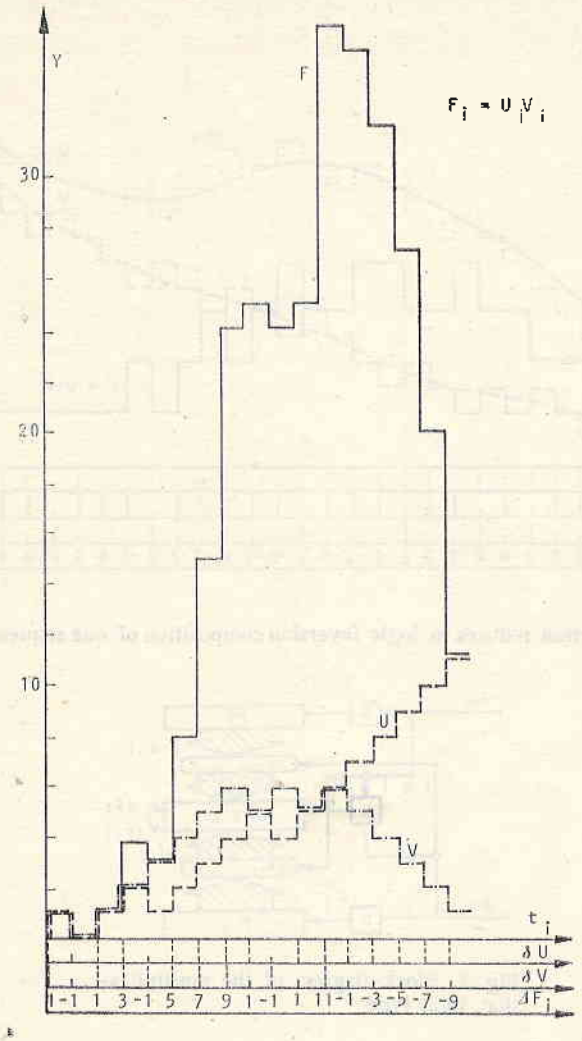

Fig. 8. The result approximations of the respective signals of the binary sequences

by DM, for instance [26, 29, 27]. Simultaneously we can measure some parameters of the subjects, such as surface [30].

Particularly interesting for these aims is the determination of uniform subjects (with respect to the spectrum) from the multispectral scan videoinformation. One of the principal requirements for such a procedure is the real time mode of the reproductive system. The DM processing system separates the uniform videoinformafional files by recording the alternative series of the output binary sequence δu [27] for each spectral channel.

By the logical intersection between the unions of the different subject chords in each channel

$$(5.8) \qquad (Uu_i^{j_1}) \cap (Uu_j^{j_2}) \cap \ldots \cap (Uu_p^{j_N}) = v$$

we obtain the homogeneous subject v, represented in the screen system by the respective restrictions of the videosignals in each channel $u_k^{j_i}$. By such separation of homogeneities it is possible to effect various types of regularization to a different extent.

6. Possibilities of Instrumental Programming in Different Modes

When designing a TV-instrument for videoinformational processing which employs a single DM processing system, it is of particular importance to minimize the instrumental part.

The introduction of instrumental programming is of specific advantage because it provides for the use of a universal module in effecting a large number and types of operations.

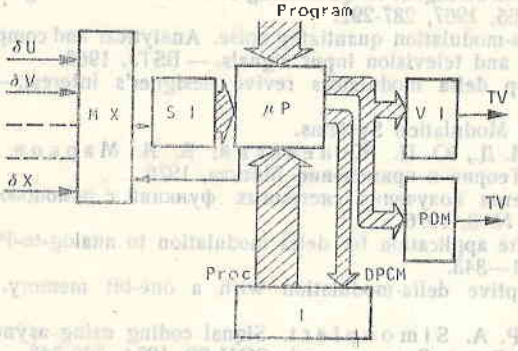

Fig. 9. The processing is effected by the microprocessor

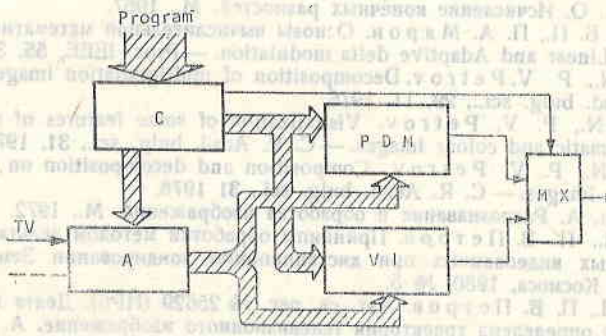

Fig. 10. The microprocessor is used as a controller

With the introduction of large integral schemes into practice, considerable possibilities to universalize the instrumental part appeared [33], e. g. the new generations of microprocessors are particularly applicable to the binary sequences, especially in analog signal processing [31]. Of course, videoprocessing sets

its specific requirements on the design of such instruments and we can divide them into two groups:

a) instruments where most of the processing is effected by the microprocessor sequences (Fig. 9);

b) instruments where the microprocessor is used only as a controller (Fig. 10).

The instruments in Fig. 9 can be successfully applied in cases when the digital streams under processing do not exceed significantly their permeability, i. e. these could be fast and high-speed bipolar microprocessors.

Inversely, the version in Fig. 10 does not require fast operation of the processor, because it commutates the instrumental part when realizing the various operations. The realization itself should be fast.

References

1. de Jager, F. Delta-modulation, a method of PCM transmission using the 1-unit code. — Philips Res. Rep., 7, 1952, 442-446.
2. O'Neal Jr. A bound on Signal-to-Quantizing Noise Ratios for Digital Encoding Systems. — Proc. IEEE, 55, 1967, 287-292.
3. O'Neal Jr. Delta-modulation quantizing noise. Analytical and computer simulation results for Gaussian and television input signals. — BSTJ, 1966.
4. Steele, R. Cheap delta modulators revive designer's interest. — Electronics, 21, 1977, 86-93.
5. Steele, R. Delta Modulation Systems.
6. Венедиктов, М. Д., Ю. П. Женевский, В. В. Марков, Г. С. Эйдус. Делта-модуляция. Теория и применение. Москва, 1976.
7. Накамура, „Метод получения системных функций с помощью дельта-модуляции". ТИИЭР, 64, № 3, 1976.
8. Goodman, D. The application for delta modulation to analog-to-PCM encoding. — BSTJ, 48, 1969, 321—343.
9. Jayant, N. Adaptive delta-modulation with a one-bit memory. — BSTJ, 49, 3, 1970, 321-342.
10. Hawkes, T. A., P. A. Simonpieri. Signal coding using asynchronous delta modulation. — IEEE Trans. Commun., vol. COM-22, 1974, 346-348.
11. Хеминг, Р. Числени методи за научни работници и инженери. С., 1974.
12. Корн, Г., Т. Корн. Справочник по математике для научных работников и инженеров. М., 1973.
13. Гельфонд, А. О. Исчисление конечных разностей. М., 1967.
14. Демидович, Б. П., П. А. Марон. Основы вычислительной математики. М., 1970.
15. Abate, J. E. Linear and Adaptive delta modulation. — Proc. IEEE, 55, 3, 1967.
16. Mishev, D. N., P. V. Petrov. Decomposition of multigradation image by isoimage. — C. R. Acad. bulg. sci.., 29, 11, 1976.
17. Mishev, D. N., P. V. Petrov. Visualization of some features of an object through monochromatic and colour images. — C. R. Acad. bulg. sci., 31, 1978, 6.
18. Mishev, D. N., P. V. Petrov. Composition and decomposition on colour and black-and-white images. — C. R. Acad. bulg. sci., 31 1978.
19. Резенфельд, А. Распознавание и обработка изображений. М., 1972.
20. Мишев, Д. Н., П. В. Петров. Принципы обработки методом дельта модуляции многозональных видеоданных при дистанционном зондировании Земли. Исследование Земли из Космоса, 1980, № 5.
21. Мишев, Д. Н., П. В. Петров. Авт. св. рег. № 25629 (НРБ). Делта модулатор, анализиращ по определена траектория телевизионното изображение. А. С. № 25629.
22. Мишев, Д. Н., П. В. Петров. Заявка за авторско свидетелство рег. № 39712, Устройство за оценка на производната на сигнал. А. С. № 273 4 (НРБ).
23. Мишев, Д. Н., П. В. Петров. Заявка за авторско свидетелство рег. № 39711, Устройство за оценка на градиента на телевизионни изображения. А. С. № 27344 (НРБ).
24. Зух, Е. Л. Недорогие универсальные преобразователи напряжения в частоту. — Электроника (русс. перевод), 1975, № 10.
25. Stanzione, D. C. Microprocessors in Telecommunication Systems. — Proc. IEEE, 66, 2, 1978.

26. Auslander, D., Y. Takahashi, M. Tomizuko. Direct Digital Process Control: Practice and Algorithms for Microprocessor Application. — Proc. IEEE, 66, 1978.
27. Fuller, S., J. Ousterhout, L. Raskin, P. Rubinfeldet al. Multi-Microprocessors: An Overview and Working Examples. — Proc. IEEE, 66, 2, 1978.

Цифровая обработка видеоинформации при помощи метода дельта-модуляции

Д. Н. Мишев, П. В. Петров

(Резюме)

В работе сделана попытка систематизировать обзор возможностей метода дельта-модуляции для осуществления некоторых операций при обработке видеоинформации. Показаны связь разностного исчисления и дельта-модуляции, а также возможности этого метода для реализации пространственно-инвариантных и масштабных трансформаций некоторых арифметических операций.

Сделана классификация обрабатывающих систем с дельта-модуляцией как по отношению к принципам работы, так и по отношению к организации аппаратной части.

BULGARIAN ACADEMY OF SCIENCES

SPACE RESEARCH IN BULGARIA, 3
Sofia · 1980

Atmospheric Spectral Transparency Analysis with Account of the Chemical Atmospheric Composition of the Friction Layer

D. N. Mishev, V. Jepa-Petrova, I. Lanzov

Observations on direct solar radiation within the visible and the near infra-red ranges make it possible to obtain series of quantities which characterize the atmospheric transparency in given spectral zones. The juxtaposition of the actual atmospheric response with the ideal optic atmospheric properties (pure and dry atmosphere) together with the chemical analysis of the air in the friction layer could result in some conclusion on the atmospheric aerozol component [1,2].

Taking all that into consideration, the direct solar radiation was observed and the aerozols of the friction layer were chemically analysed on October 23, 1977 at the reference area (Belozem) of the Plovdiv research field with "Radiometer Metrologie" 60-530, equipped with Karl-Zeiss Jena filters. The filters are consistent with the spectral intervals within which the payload is operating.

Table 1 shows the main specifics of the filters we used. As the spectrum of the direct solar radiation is taken at separate discrete points, it is assumed that the solar radiation varies within a linear regularity between two adjacent points.

In the most generalized case, the total solar energy flux, falling to the earth surface $I_0(\lambda)$ can be represented as a sum

$$I_0(\lambda) = I(\lambda) + I_{0R}(\lambda) + I_{0M}(\lambda), \tag{1}$$

where $I(\lambda)$ is the flux intensity attenuated by the atmospheric layer, $I_{0R}(\lambda)$, $I_{0M}(\lambda)$ are the intensities of the Reileigh scattered and Mie scattered radiations, respectively.

Upon direct solar radiation observations we assume that the extinction of the solar radiation when passing through the atmosphere follows Bouguer's law, which is valid for a given meteorological situation: clear and stable weather with visibility distance — $S_0 > 20$ km, i. e.

$$I_0(\lambda) = S(\lambda) \cdot e^{-\tau m} = S(\lambda) \cdot P^{m(z)}(\lambda), \tag{2}$$

where $S(\lambda)$ is the solar spectral irradiance curve, $P(\lambda)$ is the transparency spectral function, $m(z)$ is the atmospheric mass and τ is the optical atmos-

Table 1

Principal Data on the Filters Used in Ground-Based Observations of Direct Solar Radiation

No. of the filter	λ_{max} (nm)	$\Delta\lambda$ (nm)	τ %	Sensor permeability coefficient $k(\lambda)$
1	461	7.5	21	0.99
2	480	5.0	24	1.01
3	492	6.5	14	1.03
4	500	5.0	18	1.02
5	523	5.5	37	1.035
6	538	4.0	22	1.036
7	550	4.5	18	1.04
8	574	7.5	40	1.03
9	597	8.0	44	1.015
10	602	6.0	11	1.01
11	619	5.5	18	1.0
12	628	8.0	15	0.98
13	648	7.5	32	0.97
14	659	8.5	22	0.98
15	672	7.0	23	1.01
16	680	7.5	44	1.06
17	708	8.5	26	1.11
18	729	4.5	10	1.1
19	768	10	21	1.02
20	791	8	21	1.08
21	800	7.0	20	1.06
22	894	12	30	1.04
23	930	11	24	1.07
24	975	9.0	20	1.0
25	1055	15	17	0.83

pheric thickness. Those were the conditions on Oct. 23, 1977 at the reference area of Belozem.

We assume that the transparency function can be represented as a product of different multiplicands characterizing the transparency function of the different atmospheric substances. Such assumption could be true if the whole atmosphere were considered to be composed of l layers, taking into account the ammount of attenuated components, and the variation of their optical properties with the height [1].

Accordingly, expression (2) can be represented as

$$I_0(\lambda) = S(\lambda) \prod_{i=1}^{l} P_i(\lambda, m), \tag{3}$$

where l is the number of atmospheric layers with determined optical properties.

Within the considered spectral range (460-1,060 nm) such basic components could be ozone, water vapours, aerozol particles. As a result expression (3) will become

$$I_0(\lambda, m) = S(\lambda) \, . \, P_{\theta 3}(\lambda, m) \, . \, P_{H_2O}(\lambda, m) \, . \, P_M(\lambda, m) \, . \, P_a(\lambda, m). \tag{4}$$

Figure 1 shows the standard curve of spectral irradiance $S(\lambda)$ from [3], the spectral sequence of the solar radiation to the Earth surface in case of Rayleigh scattering and the variation range of the recorded direct solar radiation to the Earth surface $\Delta I_0(\lambda) = I_{0,max}(\lambda) - I_{0,min}(\lambda)$ for Oct. 23, 1977 from 10: 24 h to 14: 50 h. Figure 1 shows that the Rayleigh scatter contributes

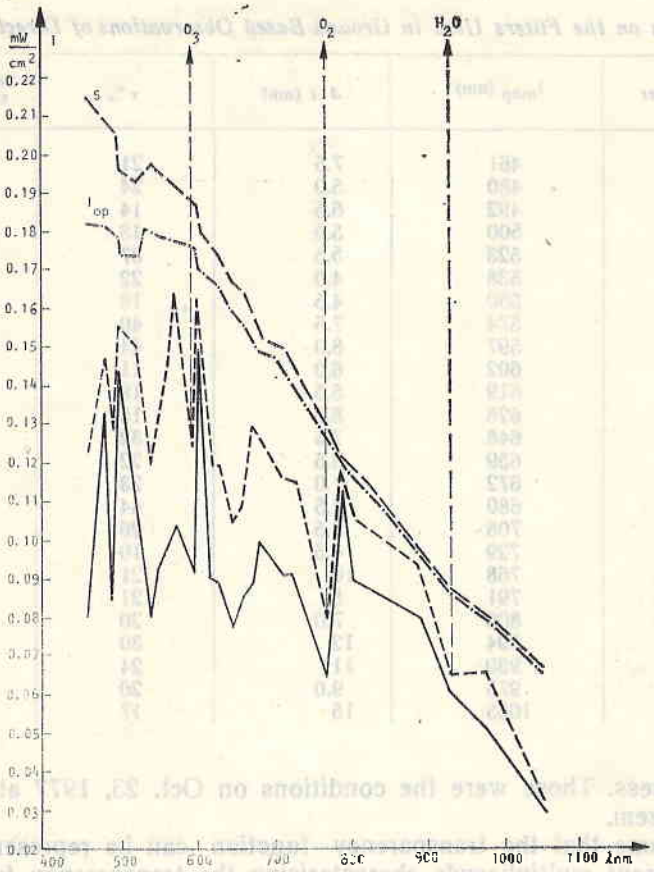

Fig. 1. Solar radiation spectral run; $S(\lambda)$ standard curve of spectral irradiance; $I_{op}(\lambda)$ spectral curve in case of Rayleigh scatter. I_{0min}, I_{0max} — minimal and maximal values of the recorded solar radiation on Oct. 23,1977

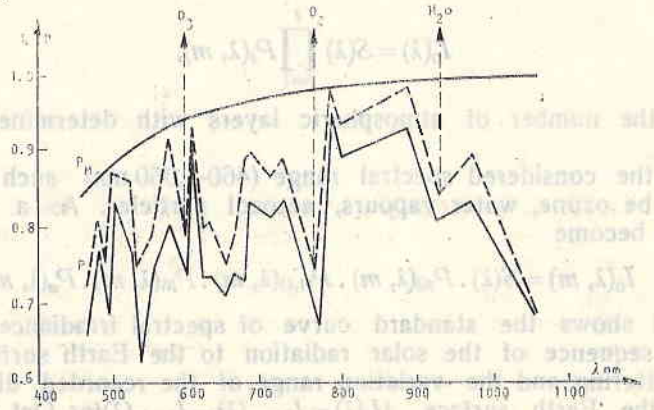

Fig. 2. Transparency spectral curves

Table 2

Composition of Some Elements in Aerosols of the Friction Layer ($\mu g/m^3$), Measured at Belozem, Plovdiv District, in November 1977

Cl^-	SO_4^{2-}	NO_3
6.04	1.97	2.5
4.85	3.38	2.4
6.40	2.23	2.0
4.40	4.63	2.8

Table 3

Results from Neutron-Activation Analysis of the Content of Some Microelements in the Atmospheric Friction Layer

No.	Litres air	Element	μg	$\mu g/m^{-3}$	%
1	4430	Al	14	3.16×10^{-3}	17.85
2	4430	Fe	10	2.26×10^{-3}	12.76
3	4430	Cu	3	6.80×10^{-4}	3.84
4	4430	Mn	28	6.32×10^{-3}	35.70
5	4430	Na	14	3.16×10^{-3}	17.85
6	4430	Co	15	3.40×10^{-4}	1.90
7	4430	Mg	≈0.1	$\approx2.00\times10^{-5}$	0.11
8	4430	Ti	7.5	1.69×10^{-3}	9.5
9	4430	Sm	0.09	2.00×10^{-5}	0.11
10	4430	Su	0.09	2.00×10^{-5}	0.11
11	4430	Rb	≈0.1	2.00×10^{-5}	0.11
12	4430	Ce	≈0.1	2.00×10^{-5}	0.11

significantly to the solar radiative attenuation within the spectral interval of 460-600 nm.

Figure 2 shows the transparency spectral curves of clear, molecular atmosphere D_M and the transparency variation range of the actual atmosphere.

The lines of oxygen absorption (684-694 nm), (729-770 nm) of the water vapours (700-740 nm), (790-840 nm) and (926-978 nm) are clearly plotted in Figs. 1 and 2. The same can be seen for the wide absorption line of O_3 with maximum of 600 nm. These results agree well with the results of [1]. The simultaneous spectral studies and the chemical analysis of the atmospheric aerosols provide description of the aerosol absorption lines in the visible spectrum.

The concentration of chlorides, nitrides, sulphates, organic and inorganic matter were derived from the aerosol chemical analysis of the friction layer. It was determined that the organic portion represents 27.77 % of the dry aerosol, while the inorganic was 72.23 %. The presence of organic matter in the friction layer defines the aerosol absorption in the visible range (Fig. 1). Tables 2 and 3 present the results from the chemical aerosol analysis of the friction layer. They show that the concentration of iron in the air is 12.8 %, which represents the fourth place with respect to the other elements after

Mn, Na and Al. The high concentration of Fe determines the high absorption capacity of the aerosols within the visible range from 0.46 to 0.68 μm, which is due mainly to the hematite and limonite in the air. This supports also the results obtained in [1]. Another portion of the absorbed radiation within the visible spectrum might be due to sulphur, to small particles of highly absorbable soot, as well as to organic atmospheric particles, as confirmed by the chemical analysis carried out by laboratory techniques.

The varying range width, characterizing the actual atmospheric transparency changes, results from atmospheric dynamic processes, which change the aerosol composition of the friction layer. Since a considerable portion of the solar radiation extinction is due to atmospheric aerosols, small variations in their composition and quantity would result in significant changes of the atmospheric transparency.

Figure 3 shows the optical thickness variations, depending on the atmospheric mass $m(z)$.

(5) $$\tau(\lambda, z) = \frac{1}{m(z)} \ln \frac{S(\lambda)}{I_0(\lambda)}.$$

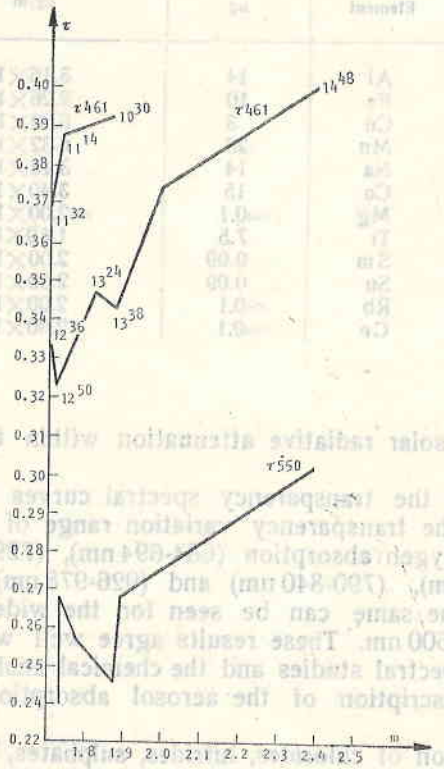

Fig. 3. Optical thickness variation τ in dependence on the atmospheric mass on Oct. 23, 1977

Figure 4 shows the atmospheric transparency variations on Oct. 23, 1977 in determined wavelengths during daytime. The transparency increase about noon with the wavelength augmentation is clearly to be seen.

Based on results from determined meteorological conditions and season, it is recommended to photograph the particular research field about noon (12:30 h) when the optical depth is minimal and the transparency is maximal

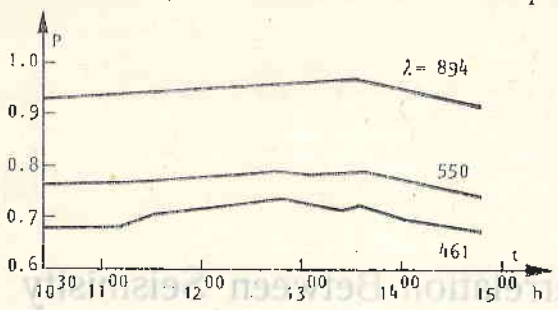

Fig. 4. Atmospheric transparency variation on Oct. 23, 1977

The results obtained show that the chemical analysis of the air in the friction layer which contributes essentially to the solar radiative attenuation, together with the optical observations on direct solar radiation, provide explanation for some spectral intervals of radiative absorption due mainly to the aerosol component in the friction layer.

References

1. Полный радиационный експеримент. Под ред. К. Я. Кондратьевой, Л., 1966.
2. Twomey, S. Atmospheric Aerosols. New York, 1977.
3. Proceedings of Symposium on Solar Radiations, Nov. 13-15, 1977.

Анализ спектральной прозрачности атмосферы с учетом химического состава атмосферы в приземном воздушном слое

Д. Н. Мишев, В. Джепа-Петрова, И. Ланзов

(Резюме)

В работе показаны результаты экспериментальных исследований спектральной прозрачности атмосферы. Полученные результаты привязаны к химическому составу атмосферы в приземном воздушном слое. Показаны спектральные интервалы поглощения солнечной радиации атмосферными газами и аэрозолем в видимом и ближнем инфракрасном диапазоне.

BULGARIAN ACADEMY OF SCIENCES

SPACE RESEARCH IN BULGARIA, 3

Sofia · 1980

On the Interrelation Between Seismisity and Fault Structures Identified by Space Image Interpretation

H. Spiridonov, E. Grigorova

Recent years are remarkable with the abundance of aerospace information in the field of geological and geomorphological research. Many papers together with the acquired observational experience confirm the understanding that a space picture could contribute to reveal some features of the deep earth crust structure. Some of the authors consider possible to determine series of buried structures from the platform fundament, as well as fault structures uplifting to Konradt and Mochorovichich surfaces [1, 6-8, and many others]. Multiple deep crust structure elements are usually determined upon others of a smaller scale, which relates to the large picture generalization of the Earth as a whole, or of separate sectors from it. This paper compares seismicity and fault structures identified by space image interpretation in scale 1:1,000,000. Most suitable for the purpose proved to be the Upper Tracian lowland and the Tundja hilly region, both known as highly seismically active regions in the Southern parts of Bulgaria [3, 5].

The American space photographs (ERTS-1) were used for that interpretation and their resolution is 90-100 m. The pictures are taken at 900 km height on Nov. 17, 1972. Images with wavelengths of 0.6 — 0.7 μm and of 0.8-1.1 μm, i. e. in the orange-red and near infrared range of the electromagnetic spectrum are most valuable for the interpretation. These pictures were published earlier [2, 9], that is why here we shall give only the scheme of interpreting the above-mentioned seismic regions.

The Maritsa seismic region overlaps with the Upper Tracian depression. This is the largest complex graben structure in the Southern part of Bulgaria, 160 km long, oriented in West-Eastern direction and up to 45 km wide from North to South. The Upper Tracian depression is a typical intermontaneous depression, formed between the intensively uplifting Rhodopean Massif and the Sredna Gora range. It is filled with upper Paleogenic and Neogene-Quaternary deposits. The Upper Paleogene is characterized by Preabone and Oligocene sediments and volcanic rocks up to 3,000 m thick. These are mainly conglomerates, sandstones, argillites, limestones, andesite tuffs and andesites. During the Neogene and Quaternary epochs, the depression considerably reduced in

size, as three additional structures developed within that format — the Plovdiv graben, the Chirpan threshold and the Zagora graben. The thickness of the younger deposits is over 300 m. The separation from the Upper Tracian crust block by adjacent morphostructures with clearly outlined fault ruptures and

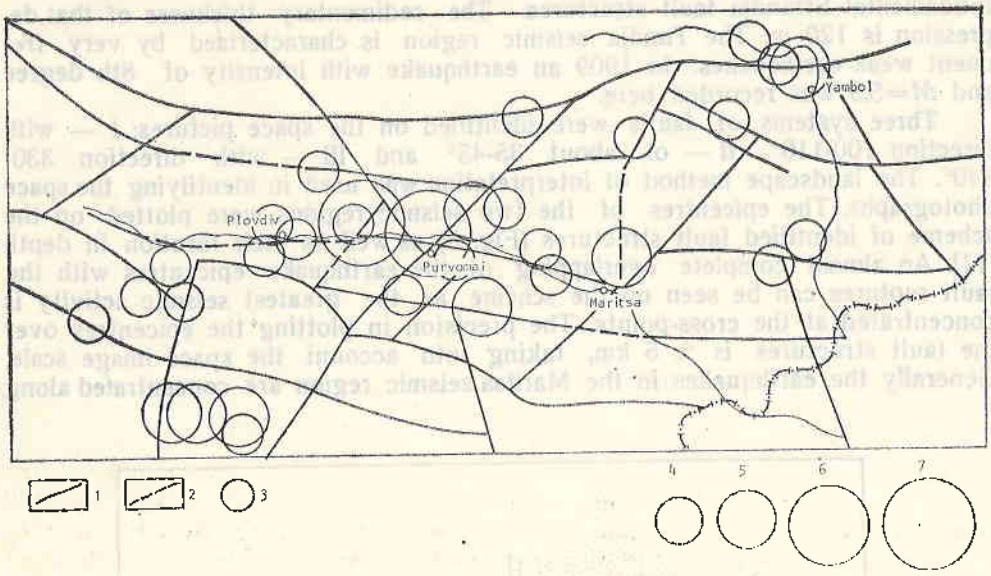

Fig. 1. Interrelations between faults identified by space pictures and earthquake epicentres in the Maritsa and Tundja seismic zones

1 — faults reliably identified by the space images; 2 — suggested faults; 3 — earthquake epicentres with M 3; 4-7 — earthquake magnitudes: 4 — M = 4.1-5; 5 — M = 5.1-6; 6 — M = 6.1-7; 7 — $M>7$

the formation of smaller block structures over that background shows the complex block structuring of the whole depression. Greater portion of these ruptures is fixed on the space pictures and is shown in the tectonic scheme. These fault structures are specific accumulative areas of significant seismic energy, which at certain periods could be released and results in earthquakes of large intensity and magnitude (Fig. 1).

The Upper Tracian depression is one of the most seismically active regions of Bulgaria. Based on historical data, we can trace there earthquakes with intensity of 9th degree in 1750 and of 7th degree in 1859. Three consequent shocks followed in 1928— on April 14— with intensity of 9th degree and magnitude $M=6.8$; on April 18 — with intensity of 9th degree and $M=7.0$ and on April 25— with intensity of 8th degree and $M=5.6$. Figure 2 shows the resultant faults from the earthquake in 1928. Two faults were structured after the shock on April 14 with $M=6.8$— Northern with 39 km of length which starts from Cherna Gora village (Plovdiv district) and continues eastward up to Chirpan and Southern, which overlaps with Maritsa river bed. It starts from Purvomay and reaches Dimitrovgrad eastward. Other faults were ruptured during the second shock on April 18 with $M=7.0$. The main fault is located at 10 km westward from Purvomay and follows to North-Western direction. The total length of the faults resulting from the two shocks is up to 105 km. The largest depression locates northward from the line Chalakovo village (Plovdiv district) — Purvomay at about 3 m and southward

that line we trace an uplift to 0.4 m [10]. Some of the faults structured after the earthquake in 1928 were identified on the space pictures as in certain areas they overlap completely with the actual structures (Fig. 2).

The Tundja seismic region which comprises the hilly area between Yambol and Elhovo along the Tundja river is a part of the Elhovo depression, the latter being a young Neogene-Quaternary structure, formed transversely to the fundamental Strandja fault structures. The sedimentary thickness of that depression is 120 m. The Tundja seismic region is characterized by very frequent weak earthquakes. In 1909 an earthquake with intensity of 8th degree and $M=5.9$ was recorded here.

Three systems of faults were identified on the space pictures: I — with direction 100-110°, II — of about 35-45° and III — with direction 330-340°. The landscape method of interpretation was used in identifying the space photographs. The epicentres of the two seismic regions were plotted on the scheme of identified fault structures (Fig. 3) as well as their location in depth [11]. An almost complete overlapping of the earthquake epicentres with the fault ruptures can be seen on the scheme as the greatest seismic activity is concentrated at the cross-points. The precision in plotting the epicentres over the fault structures is ± 5 km, taking into account the space image scale. Generally the earthquakes in the Maritsa seismic region are concentrated along

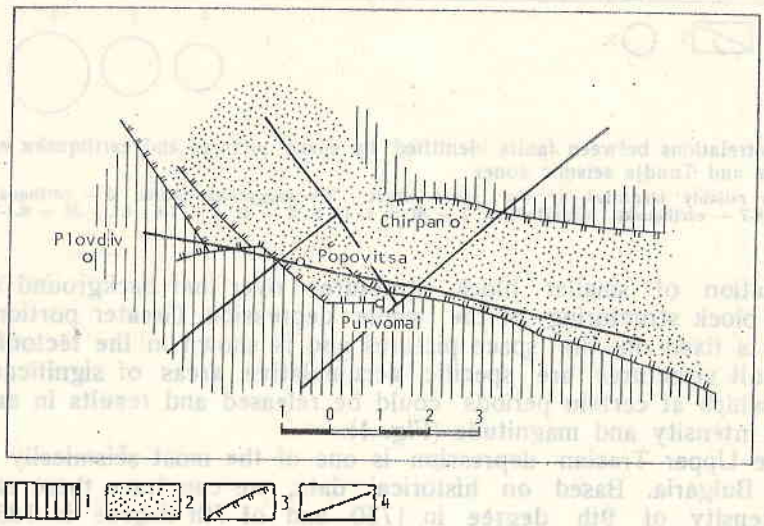

Fig. 2. Scheme of a part of the Maritsa seismic region between Plovdiv and Purvomay

1 — the sunk part of the Thracian lowland after the earthquake in April 1928 (more than 3 m); 2 — the uplifted part of the lowland after the earthquake with 0.4 m; 3 — faults identified on the space pictures; 4 — actual faults formed during the earthquake in 1928

the Maritsa river flow between Pazardjik and Purvomay at a distance of 100 km and 40 km width. In the other seismic region they are concentrated along the Tundja river flow between Yambol and Elhovo and about the Monastery uplifts. The vertical profile of the same scheme plots the earthquakes by amplitude. It can be seen that the earthquake epicentres are mostly at the

depths of Konradt boundary or in the granite layer of the earth crust. Only few of them reach the Mocho boundary. The thickness of the earth crust in the two seismic regions varies betwen 35 and 42 km. The greatest thickness of the earth crust is within the limits of the Chirpan treshold. At the same time, this earth crust block is seismically most active.

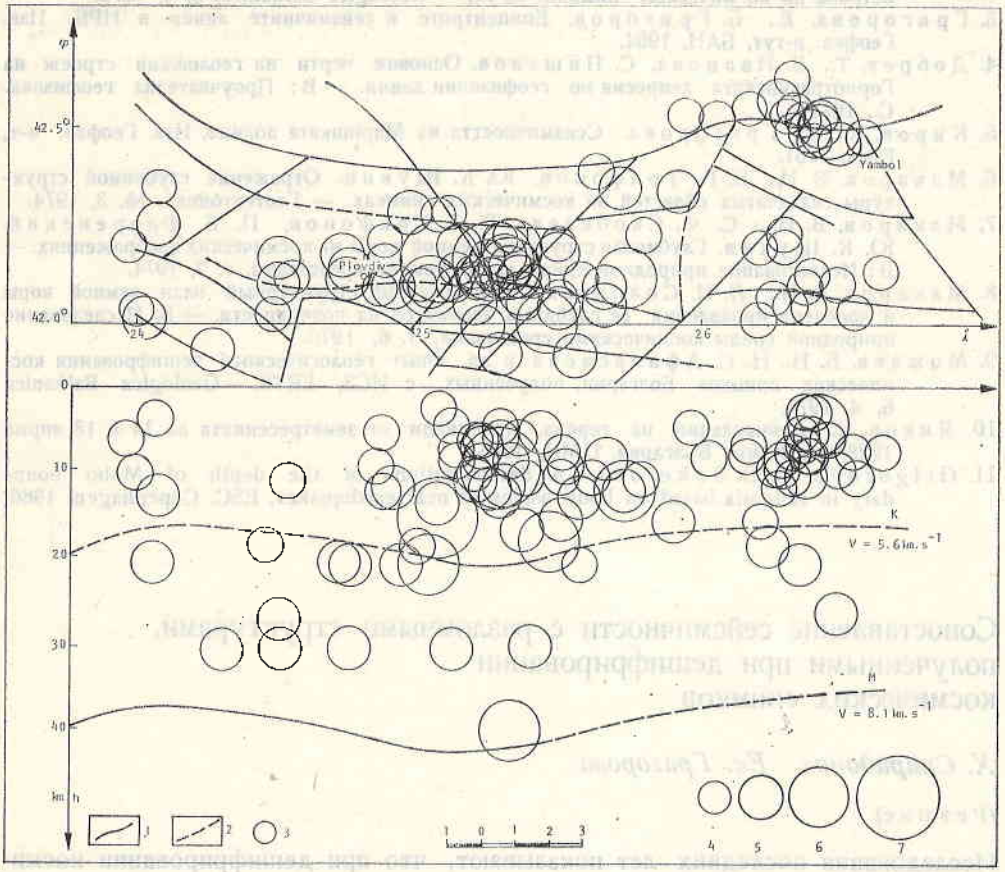

Fig. 3. Scheme of the identified fault structures and the earthquake epicentres, the focal depth being also given

Above: 1 — faults reliably identified on the space pictures; 2 — assumed faults; 3 — earthquake epicentres with $M > 3$; Below: 4 — $3 \leq M \leq 4$; 5 — $4.1 \leq M \leq 5$; 6 — $5.1 \leq M \leq 6$; 7 — $6.1 \leq M \leq 7$

The complex inner block-fault structuring of the Upper Thracian complex depression which is confirmed by the geophysical investigation [4] is reflected in the earth surface relief. This relief is mainly observed on the space pictures. Therefore, the summing effect from the tectonic movements of the earth crust, including the deep layers, would be reflected "enlightened" in the relief. The overlap of the fault structures identified from the space photographs with the epicentres of the earthquakes in the Maritsa and Tundja seismic regions shows that reliable information on the deep earth crust structure could be obtained. In our case, this information goes as far as the Mochorovichich boundary.

References

1. Ананин, И. В., В. Г. Трифонов. Сопоставление сейсмичности с элементами дешифрирования космических изображений.— В: Исследование природной среды космическими средствами, т. 5. М., 1976.
2. Гочев, П. Новые данные о разломной тектонике Болгарии и части Балканского полуострова по космическим снимкам, ЕРТС — Geologica Balkanica, 6, 4, 1976.
3. Григорова, Е., Б. Григоров. Епицентрите и сеизмичните линии в НРБ. Изв. Геофиз. и-тут, БАН, 1964.
4. Добрев, Т., В. Иванова, С. Пищалов. Основни черти на геоложкия строеж на Горнотракийската депресия по геофизични данни. — В: Проучвателна геофизика. С., 1972.
5. Киров, К., Е. Григорова. Сеизмичността на Маришката долина, Изв. Геофиз. и-т, БАН, 1961.
6. Макаров, В. И., В. Г., Трифонов, Ю. К. Щукин. Отражение глубинной структуры складчатых областей на космических снимках. — Геотектоника, №, 3, 1974.
7. Макаров, В. И., С. Ф. Скобелев, В. Г. Трифонов, П. В. Флоренский, Ю. К. Щукин. Глубинная структура земной коры на космических изображениях. — В: Исследование природной среды космическими средствами, т. 2, 1974.
8. Макаров, В. И., Л. И. Соловьева. Перекрастный структурный план земной коры и проблема проявления ее глубиных элементов на поверхности. — В: Исследование природной среды космическими средствами, т. 6, 1976.
9. Можаев, Б. Н., Н. С. Афанасиева и др. Опыт геологического дешифрования космических снимков Болгарии, полученных с ИСЗ, ERTS. — Geologica Balkanica 6, 4, 1976.
10. Янков, К. Денивелации на терена, причинени от земетресенията на 14 и 18 април 1928 г. в Южна България, ЦМИ, 1945.
11. Grigorova, E., D. Sokerova. A determination of the depth of Moho boundary in Bulgaria based on body waves of near earthquakes. ESC. Copenhagen, 1966.

Сопоставление сейсмичности с разломными структурами, полученными при дешифрировании космических снимков

Х. Спиридонов, Ек. Григорова

(Резюме)

Исследования последних лет показывают, что при дешифрировании космических снимков вполне возможно вскрыть элементы глубинного строения земной коры. Для исследования этой возможности были дешифрированы космические снимки, и полученные разломы были сопоставлены с эпицентрами землетрясений в Верхнефракийской низменности и в Тунджанской холмистой области, известных как сильно сейсмические районы Южной Болгарии. Результаты сопоставления показывают, что разломные структуры, выявленные на космических изображениях, отражают глубинное строение земной коры до границы Мохоровичича.

BULGARIAN ACADEMY OF SCIENCES

SPACE RESEARCH IN BULGARIA, 3

Sofia · 1980

Interferential Filters in Spectral Instruments without Collimation Optics

K. P. Bakalova

Interferential filters hold an important place among the apparatuses for spectral measurements. It is known by now that their transmission can be described by the function [1]

$$(1)\qquad \tau(\lambda, \theta)=\frac{I^{(t)}}{I^{(i)}}=\left(1-\frac{A}{1-R}\right)^2\cdot\frac{1}{1+F\sin^2\frac{\delta(\lambda,\theta)}{2}},$$

where

$$(2)\qquad \delta(\lambda, \theta)=\frac{4\pi}{\lambda}nh\cos\theta'+2\varphi$$

is the phase difference between two beams, one of which has had a double inner reflection more than the other. The following symbols have been applied in these expressions:

θ' — angle of refraction in the filter;
n — index of refraction of the intermediate layer of the filter;
h — thickness of the intermediate layer;
φ — phase shift upon inner reflection from metal coatings;
λ — wavelength in vacuum;
$A(\theta)$ — absorption or diffraction of light, accordingly in the metal or polylayer dielectric reflecting coatings of the filter;
$R(\theta)$ — reflecting capacity of the coatings, and $F=\frac{4R}{(1-R)^2}$.

If we accept the index of refraction of the air for 1, then

$$\cos\theta'=\sqrt{1-\frac{\sin^2\theta}{n^2}},$$

where θ is the angle of fall of the light beam to the filter. Expressions (1) and (2) are valid when a parallel shaft of beams falls on the filter. Consequently, the position of the maximum in the admission band depends on the decline of the beams to the normal to the surface of the filter

$$\lambda_m(\theta)=\frac{2nh}{m-\varphi/\pi}\sqrt{1-\frac{\sin^2\theta}{n^2}},\quad m=1, 2, \ldots,$$

where the decline is expressed by θ.

On increasing the degree of θ the maximum of admission shifts in the direction of the shorter wavelengths. As a matter of principle, the interferential filters are designed for operation with a parallel shaft of light, falling almost horizontally to their surface. For that reason the characteristics con-

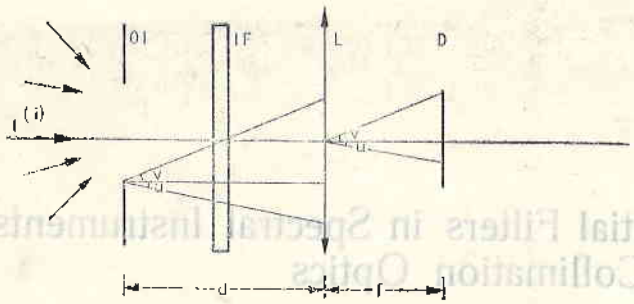

Fig. 1. Optical part of the spectral instrument: OI — optical inlet; IF — interferential filter; L — lens; D — detector

tained in their certificates are for such conditions of operation. In some of the apparatuses for spectral measurements, however, in view of considerations of energy and design, the interferential filters have to operate with non-parallel shafts of light, e. g. in the portable spectrometers for measurements of the spectral reflecting characteristics of some natural formations. The dependence of the position of the maximum in the admission band of the angle of fall limits the angular aperture of the filtered shafts of light [2]. It is not always possible to keep to this limit in practice. In order not to lose the accuracy of measurements, an evaluation of the differences could be made between the performance of interferential filters with a parallel shaft of light, falling normally on their surface, and when working with non-parallel shafts of light at an angle of θ_m. In its most general and simplified form the optical part of the spectral instrument may pe presented as a combination of optical inlet (OI) with a certain aperture through which the measured flow of light enters the instrument; an interferential filter (IF) which admits the light flow in a determined spectral range; a lens (L) which focuses the filtered light on the light-sensitive surface of the detector (D) — a photoelectron converter (Fig. 1). We shall be interested in the signal at the outlet of the detector in both cases — upon lighting the filter with parallel and non-parallel shafts of light.

The light entering the instrument may be considered as a super-position of flat monochromatic waves with length λ, spreading at an angle θ to the optical axis of vision of the system (the normal to the surface of IF, L and D). The intensity of these waves falling on the filter is $I^{(i)}(\lambda, \theta)$.

If it is accepted that the natural objects reflect light diffusely [3], we may consider $I^{(i)}$ as independent on θ. The measurement of $I^{(i)}$ is in a narrow range which is determined by the admission band of the filter. In that range we may consider $I^{(i)}$ as a constant on λ, but its value is determined from its place in the spectrum, i. e. $I^{(i)}(\lambda, \theta) - I_\lambda^{(i)}$. The change in the intensity of each monochromatic wave after its transition through the IF is described by the function (1). Spreading in the afterfilter space are flat monochromatic waves with intensity $L^{(i)}(\lambda, \theta) = I_\lambda^{(i)} \tau(\lambda, \theta)$. We believe that there is no interference

between the waves with different λ and that it is possible to neglect the interference between the monochromatic waves spreading at different angles θ in the space after the filter. Then the intensity of the field at each point from the surface of the lens will be the sum of the intensities of all flat monochromatic waves reaching that point. The detector is affected only by these waves for which the angle $\theta \in (0, v)$, where v is determined by the relation $v = \operatorname{arctg} \frac{r_D}{f}$. The energy flow coming to the detector is equal to that of the lens, formed from all waves spreading in the direction θ, with $0 < \theta < v$ (if we neglect the losses in the lens). The signal at the output of the detector is proportional to that flow of energy crossing the light-sensitive surface: $dU = S(\lambda, \theta, P) d\Phi$, where $S(\lambda, 0, P)$ is the sensitivity of the detector, which generally depends on the wave-length λ, the angle of fall θ, and the spot on the light-sensitive surface (point P). In order to simplify, we may assume that S does not depend on the coordinates of the point P and also that it is a constant in the range considered. The dependence on the angle θ is frequently accepted to be a Π-like function, i. e.

$$S(\theta) = \begin{cases} S(0), & \theta < \theta_0 \\ 0, & \theta > \theta_0 \end{cases}.$$

Taking into account the above considerations about the output signal of the detector, we come to the expression

$$U = \frac{c}{2} S \int_0^{\infty} \int_0^{\theta_m} B(\theta) I^{(\theta)}(\lambda, \theta) \sin\theta \cos\theta \, d\theta \, d\lambda, \tag{3}$$

where: θ_m is the more acute of the angles v and θ_0,
c is the speed of light in vacuum,
$B(\theta)$ is the section of the surface of OI and that of L, when OI is projected at angle θ in the plane of L. Let us assume that the following condition has been fulfilled:

$$r_D = f \frac{r_L - r_{OI}}{d}.$$

In that case $B(\theta) = \text{constant}$ and the output signal is expressed by

$$U = \frac{c}{2} sB \int_0^{\infty} I_\lambda^{(\theta)} \int_0^{\theta_m} \tau(\lambda, \theta) \sin\theta \cos\theta \, d\theta \, d\lambda = \frac{c}{2} sB \int_0^{\infty} I_\lambda^{(\theta)} f(\lambda) d\lambda, \tag{4}$$

where θ_m is equal to the smaller of the angles θ_0 and u. The spectral range through which the intensity has been measured is determined from the type of the function $f(\lambda)$. In the above assumptions $f(\lambda)$ is determined from the characteristics of the filter. In other concrete cases it is possible that the quantities S and B will remain under the digit of the integral on θ, i. e. they will also influence the final result from the measurement of $I^{(\theta)}$. Here is an investigation of the function

$$f(\lambda) = \int_0^{\theta_m} \left(1 - \frac{A}{1-R}\right)^2 \frac{\sin\theta \cos\theta}{1 + F(\theta) \sin^2 \frac{\delta(\lambda, \theta)}{2}} \, d\theta \tag{5}$$

Table 1

	1F, K=1.8		2 F, k=2.6		3 F, k=1.4		4 F, k=1.5		5 F, k=1.15		5 F, k=1.65	
Θ^0	$\tau_m(\theta)\%$	$\Delta\%$	$\tau_m(\theta)\%$	$\Delta\%$	$\tau_m(\theta)\%$	$\Delta\%$	$\tau_m(\theta)\%$	$\Delta\%$	$\tau_m(\theta)\%$	$\Delta\%$	$\tau_m(\theta)\%$	$\Delta\%$
0	43.0	0.0	25.5	0.0	50.0	0.0	30.5	0.0	25.0	0.0	22.5	0.0
5	42.5	0.0	25.0	0.6	50.0	0.7	30.5	0.9	25.0	0.5	22.5	1.0
10	41.0	0.2	23.0	0.3	49.0	1.0	29.5	0.1	24.5	0.0	21.5	0.4
15	38.5	0.3	20.0	1.3	47.0	0.6	28.5	1.0	24.0	0.5	20.0	2.1
20	34.5	0.9	15.5	0.7	43.5	1.5	26.5	1.6	23.0	0.1	19.0	0.5

for different values of the angle θ_m and for the parameters of the filter. The quantities A and R, and consequently F, are functions of θ, and it is difficult to provide a precise analytical expression. It is clear from (1) that the term $\tau_m(\theta)=\left(1-\frac{A}{1-R}\right)^2$ represents the maximum value of the admission of IF, when lit with a parallel shaft of light falling at an angle of θ to the normal of its surface. This provides an opportunity to determine the dependence $\tau_m(\theta)$ for each filter. Such measurements were carried out for two types of IF by means of Perkin Elmer spectrometer with spectral resolution of 1 nm, which draws the function of admission of the filters from the wavelength. We have the curves of admission for every filter corresponding to lighting up with a parallel shaft of light falling in angles changed every five degrees. The results from the measurements are given in Table 1. The dependences $\tau_m(\theta)$ for all filters approximate well with the function cos $(K\theta)$ at angles $\theta\leq 20°$, where the constant K is different for the different filters and has values of 1.15 to 2.65. The error in the approximation is also given in Table 1.

It may be accepted that the angular aperture of the instruments rarely exceeds 20 degrees, and for that reason it is not necessary to follow the dependence $\tau_m(\theta)$ further. The result is that for almost all filters $\tau_m(35°)<\frac{1}{2}\tau_m(0°)$; a split curve of admission occurring in some bigger values of θ, due to the polarization of light.

It is possible to see the change in the quantity of F with the change of θ in these experimental curves after the formula

$$F(\theta)=\frac{\tau_m(\theta)-\tau(\theta)}{\tau(\theta)\sin^2\frac{\delta(\lambda,\theta)}{2}},$$

which follows directly from (1). The value of $\tau(\theta)$ corresponds to a certain λ. It is assumed that $\varphi=0$, which may occur in filters with reflecting coatings made of polylayer dielectric. It is obvious from (2) that $nh=\frac{\lambda_m(0)}{2}$, if we accept $m=1$. $\lambda_m(0)$ is the length of the wave for which the filter has maximum admission when lit up with a parallel shaft of light. This calculation can be carried out very accurately, because the function $\sin^2\frac{\delta(\lambda,\theta)}{2}$ changes rapidly about its maximum value $\tau_m(\theta)$, but it nevertheless proves that $F(\theta)$ does not change very much. Here are the results of the calculations for one of the filters:

θ^0	0	5	10	15	20
F	122	132	121	134	117

We shall accept that F=const. when calculating the integral (5). The results are given in Table 2. They show that the bigger the index of admission of the intermediate layer of the filter, the less significant the shift of the admis-

Table 2

n'	F	k	θ_m^0	λ_m/λ_0	$\Delta\lambda_m/\lambda_0$	$\Delta\lambda_{HW}/\lambda_0$	$f_{max} \cdot 10^{-2}$
1.5	120	1.5	5	0.9987	0.0013	0.0292	0.3772
1.5	120	1.5	10	0.9950	0.0050	0.0307	1.4258
1.5	120	1.5	15	0.9890	0.0109	0.0366	2.7318
1.5	120	1.5	20	0.9818	0.0182	0.0490	3.7214
2.0	120	1.5	5	0.9990	0.0009	0.0291	0.3776
2.0	120	1.5	10	0.9962	0.0037	0.0300	1.4496
2.0	120	1.5	15	0.9918	0.0082	0.0335	2.9150
2.0	120	1.5	20	0.9860	0.0140	0.0413	4.2363
4.0	120	1.5	5	0.9995	0.0005	0.0291	0.3780
4.0	120	1.5	10	0.9981	0.0019	0.0293	1.4737
4.0	120	1.5	15	0.9959	0.0041	0.0302	3.1360
4.0	120	1.5	20	0.9929	0.0071	0.0324	5.0488
1.5	200	1.5	5	0.9987	0.0013	0.0226	0.3766
1.5	200	1.5	10	0.9950	0.0050	0.0246	1.3923
1.5	200	1.5	15	0.9891	0.0109	0.0317	2.5185
1.5	200	1.5	20	0.9822	0.0177	0.0455	3.2359
1.5	120	2.0	5	0.9987	0.0013	0.0292	0.3760
1.5	120	2.0	10	0.9950	0.0050	0.0307	1.4068
1.5	120	2.0	15	0.9892	0.0108	0.0366	2.6501
1.5	120	2.0	20	0.9826	0.0174	0.0488	3.5310
1.5	120	2.5	5	0.9987	0.0013	0.0292	0.3745
1.5	120	2.5	10	0.9950	0.0050	0.0307	1.3824
1.5	120	2.5	15	0.9895	0.0105	0.0366	2.5472
1.5	120	2.5	20	0.9836	0.0164	0.0486	3.2817

Table 3

θ_m^0	λ, nm / $\Delta\lambda_m$ $\Delta\lambda_{HW}$, nm	400	500	600	700	800
0	$\Delta\lambda_{HW}$	11.66	14.58	17.50	20.41	23.33
5	$\Delta\lambda_m$	0.52	0.65	0.78	0.91	1.04
	$\Delta\lambda_{HW}$	11.68	14.60	17.52	20.44	23.36
10	$\Delta\lambda_m$	2.00	2.50	3.00	3.50	4.00
	$\Delta\lambda_{HW}$	12.28	15.35	18.42	21.49	24.56
15	$\Delta\lambda_m$	4.36	5.45	6.54	7.63	8.72
	$\Delta\lambda_{HW}$	14.64	18.30	21.96	25.62	29.28
20	$\Delta\lambda_m$	7.28	9.10	10.92	12.74	14.56
	$\Delta\lambda_{HW}$	19.60	24.50	29.40	34.30	39.20

sion band, while the half-width of the latter is narrower. The filters with greater reflecting capacity of the coatings R (consequently F is larger also) give narrower admission bands. The influence of the constant K in the dependence of maximum admission of the angle of fall θ: $\tau_m(\theta)=\cos(K\theta)$ over the change

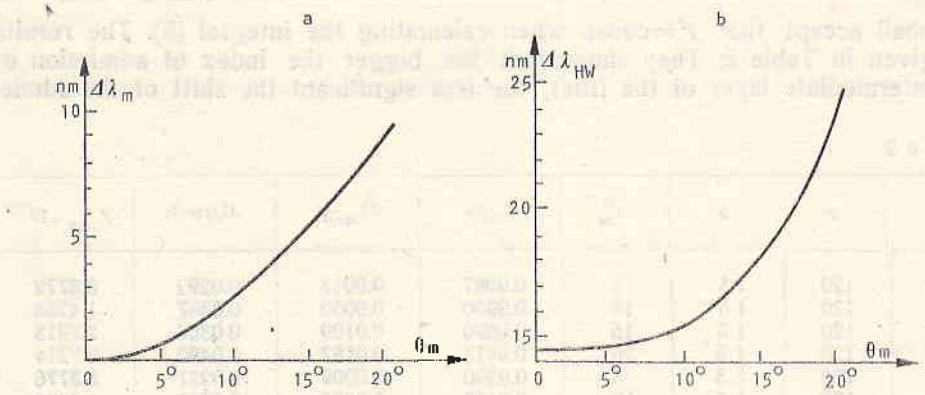

Fig. 2. Dependences of $\Delta\lambda_m(\theta)$ and $\Delta\lambda_{HW}(\theta)$ for $\lambda_0=500$ nm

of the admission band is negligible. When choosing the parameters of the filters, the maximum shift occurs for the combination of values: $n=1.5$; $K=1.5$; and $F=120$. The shift of the maximum $\Delta\lambda_m$ and the half-width of admission band for a filter with such parameters on different wavelengths λ and for shafts of light with different angle θ_m are given in Table 3. The shift of the maximum in the admission band $\Delta\lambda_m$ and the half-width of the band increase parallel with the increase of the angle θ_m. The dependences $\Delta\lambda_m(\theta)$ and $\Delta\lambda_{HW}(\theta)$ for $\lambda_0=5{,}000$ A are presented on Fig. 2.

It is evident from the above that there exists a certain change in the measured spectral range depending on the working regime of the IF. This change may either be neglected or taken into consideration, depending on the precision necessary for the particular measurements.

References

1. Borne, M., E. Wolf. The Fundamentals of Optics. M., 1973.
2. Seidel, A., G. Ostrowskaya, Y. Ostrovski. Spectrography. M., 1974.
3. Kuchko, A. S. Aerophotography. M., 1974.

Интерференционные фильтры в спектральных приборах без колимирующей оптики

К. П. Бакалова

(Резюме)

Характеристики интерференционных фильтров являются функциями угла падения света. В статье рассмотрена работа интерференционных фильтров со сходящими световыми пучками. Показаны смещение максимума и изменение полуширины полосы пропускания при изменениях углов сходимости пучков в интервале 0—20°.

BULGARIAN ACADEMY OF SCIENCES

SPACE RESEARCH IN BULGARIA, 3

Sofia · 1980

Current-Voltage Nonampere Transformer with Automatic Switching of the Measurement Range

M. N. Gousheva

The need to measure current variations within a large dynamic range in space probe experiments should be matched by reliability (maximum simplicity of the equipment) and by information restriction (minimum number of telemetric channels used). The switching of the sensitivity scales of the DC measuring tract of the spaceborn service equipment when the rocket attains a definite altitude involves a certain hazard. Such switching at an inappropriate moment results in loss of useful information due to insufficient dynamic range of the electron block.

That is why it is necessary to switch the range in accordance with the concrete situation (charge carriers density in space plasma) [1]. The availability of only one channel providing information as well as two sensitivity scales covering a dynamic range of 10^3 (in case of measurements with meteorological rockets) imposes certain restrictions on the transformer design.

The block circuit of the DC measuring tract (current-voltage transformer, Fig. 1) satisfies the above requirements. The circuit consists of a DC amplifier (DCA), a comparator (C), a repeater (R), and a switching device (S). When collector current from a spherical ion trap is applied to the DCA input, it is transformed into U_2 voltage and enters the telemetric channel (TMS). The entire DCA divider is switched on at the initial moment, because the range has to be selected regardless of the magnitude of the input current. $U_{z1} = -10$ V is applied to the non-inverting input of C. The electron keys are in the following positions: K_1 — open, K_2 — closed, and K_3 — open. The three possible cases under these conditions are: (1) The V-A characteristics is entirely described within the sensitive scale (Fig. 2 — sector a_1). This sector corresponds to a region of very low densities. The DCA range is not switched. (2) The V-A characteristics is described both within the sensitive and the coarse scales due to the sensitive scale saturation at a given moment (Fig. 2 — sector b_1). This is the case of high-density measurements. At $U_1 = -10$ V (saturation of the sensitive scale), C is actuated and S sets the keys as follows: key 1 — closed (the DCA coefficient of amplification decreases ten times), key 2 — open, key 3 — closed ($U_{z2} = -0.5$ V). (3) The V-A characteristics is fully described

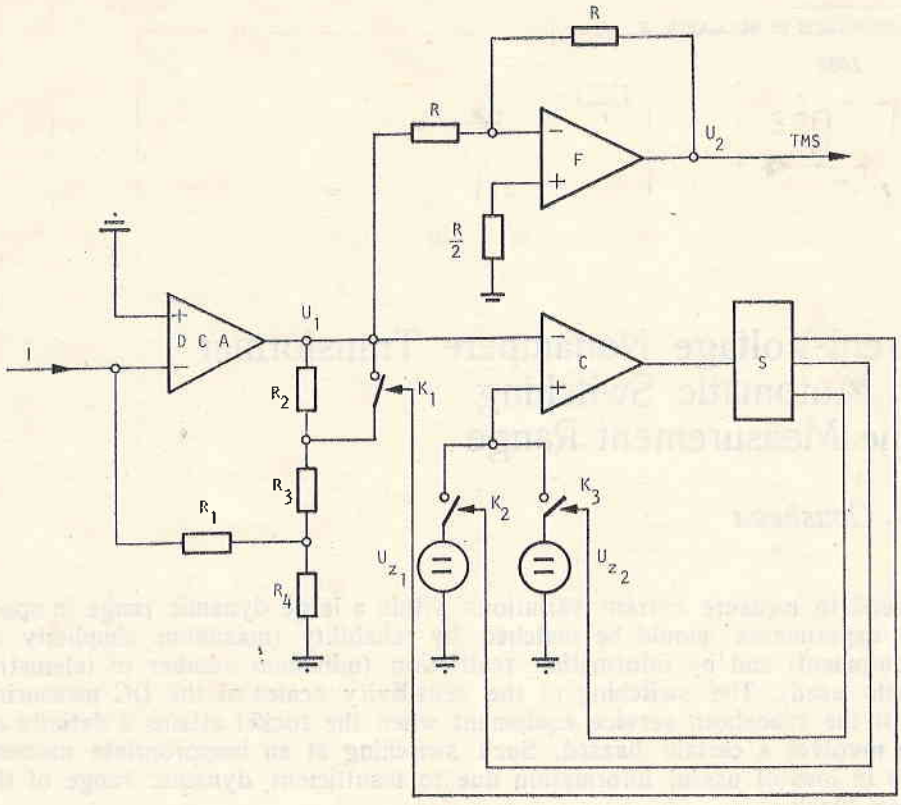
R
R
F
U2
TMS
R/2
D C A
U1
I
R2
K1
C
S
R3
K2
K3
R1
Uz1
Uz2
R4

Fig. 1

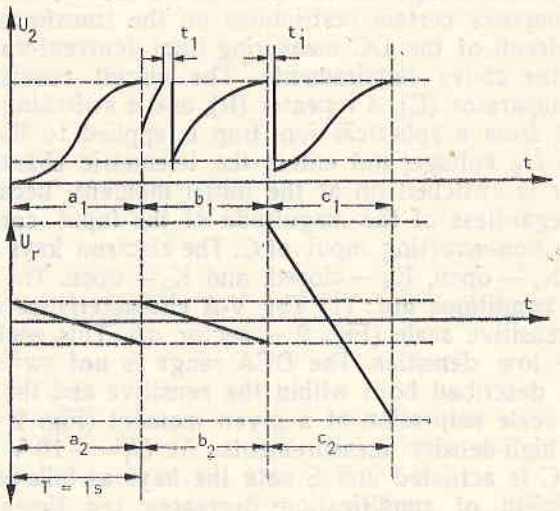
U2
t1
t1
t
a1
b1
c1
Ur
t
a2
b2
c2
T = 1s

Fig. 2

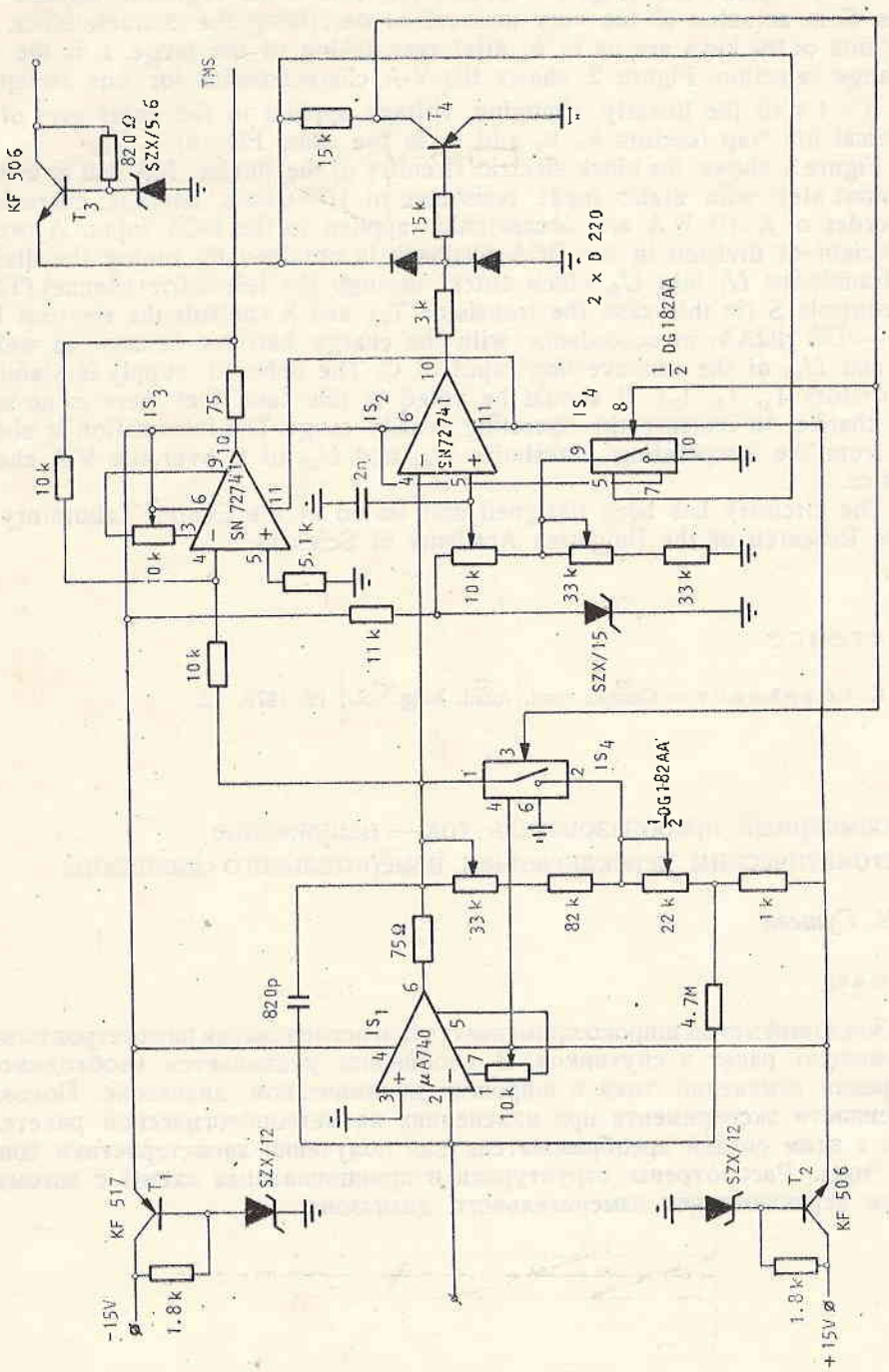
KF 506
T3
820 Ω
SZX/5.6
TMS
15 k
T4
15 k
2 x D 220
3 k
1/2 DG182AA
IS3
75
IS2
10
SN72741
IS4
8
10 k
9
10
SN 72741
2n
10 k
33 k
33 k
5.1 k
11 k
SZX/15
10 k
IS4
1/2 DG182AA
33 k
82 k
22 k
1 k
75 Ω
820p
IS1
μA740
4.7M
10 k
SZX/12
SZX/12
KF 517
T1
T2
KF 506
-15V
1.8 k
1.8 k
+15V

Fig. 3

within the coarse scale (Fig. 2 — sector c_1). This is the region of highest densities. C is actuated at the very moment of describing the characteristics. The positions of the keys are as in b_1 after reswitching of the range. t_1 is the time of range selection. Figure 2 shows the V-A characteristics for one sweep period $T=1$ s of the linearly changing voltage applied to the outer grid of the spherical ion trap (sectors a_1, b_3 and c_2 in the same Figure) — U_r.

Figure 3 shows the block electric circuitry of the device. MA 740 is used as an input step with static input resistance of 10^{12} Ohms, because currents of the order of $X.10^{-10}$ A are occasionally applied to the DCA input. A precise coefficient of division in the DCA feedback is obtained by tuning the divider. IS_3 transforms U_1 into U_2, which enters through the telemetric channel (TMS), IS_2 controls S (in this case the transistor T_4), and S controls the electron keys (IS_4) — DG 182AA, in accordance with the charge carriers density, as well as U_{z1} and U_{z2} of the noninverting input of C. The onboard supply is stabilized (transistors T_1, T_2, T_3). It should be noted in this case that there is no separate channel to indicate the operating sensity range. This information is obtained from the cooperating thresholds U_{z1} and U_{z2} of C over the V-A characteristics.

The circuitry has been designed and tested at the Central Laboratory for Space Research of the Bulgarian Academy of Sciences.

Reference

1. S. K. Chapkunov. — Compt. rend. Acad. bulg. sci., 19, 1976, 12.

Наноамперный преобразователь ток — напряжение с автоматическим переключением измерительного диапазона

М. Н. Гушева

(Резюме)

Зондовый метод широко применяется при исследовании параметров плазмы с помощью ракет и спутников. В сообщении указывается необходимость измерения изменений тока в широком динамическом диапазоне. Показаны особенности эксперимента при изменениях на метеорологической ракете. В связи с этим создан преобразователь для получения характеристики зондового тока. Рассмотрены структурная и принципиальная схемы с автоматическим переключением измерительного диапазона.

BULGARIAN ACADEMY OF SCIENCES

SPACE RESEARCH IN BULGARIA, 3

Sofia · 1980

Sweep Generator for Probe Experiment Onboard Meteorological Rocket

T. N. Ivanova

The velocity and maximum altitude of meteorological rockets, e. g. of the "Centaurus" type [1], are much smaller in comparison with those of the geophysical rockets, e. g. of the "Vertical" type. Whereas at an altitude of $H = 100$ km the velocity of meteorological rockets is about 1 km/s and they reach an altitude of $H_{max} = 150 \div 180$ km, the rockets we use for probe experiments reach an altitude of $H_{max} = 1{,}510$ km and at $H = 100$ km their velocity is about 8 km/s [2, 3].

The principle of operation of the block circuits of the Bulgarian measurement instruments launched until now in irrecoverable containers of the geophysical rockets "Vertical" 3, 4 and 6 (in 1975, 1976 and 1977) are given in [4, 5]. In an experiment with a meteorological rocket a full V-A characteristics from the collector of a spheric ion trap (SIT) from retarding to saturation region may be obtained at much smaller voltage amplitudes of the sweep voltage of the outer grid of a trielectrode SIT (U_{SIT}) in comparison with the amplitudes used until now of $U_{SIT} = (+15 \div -5)$ V [6].

According to our calculations, the necessary voltage U_{SIT} is symmetric to the zero (container body) with an amplitude $(+1 \div -1)$ V. As the potential to which the body will be charged may reach $+3 \div 4$ V, a saw-tooth voltage (wave) generator (SWG) circuit is used for obtaining U_{SIT} with a variable amplitude — over a period of U_{SIT} $(+5 \div -5)$ V.

Besides that, the service control system in experiments with meteorological rockets is simplified — there are no onboard commands for simultaneous as well as synchro-impulses.

The telemetric system is also of limited capacity, and the sweep voltage U_{SIT} is not telemetrically controlled, as had been the case in the experiments carried out until now.

Consequently, in the design of a SWG we must pay attention first of all to the amplitude stability of the voltage generated, because instability in the period may be judged from the duration of the V-A characteristics clearly differentiated from one another.

In accordance with the above requirements on the qualities of the sweep generator for SIT installed on a meteorological rocket, we propose an amplitude-stabilized symmetric SWG made with integrated circuits. The complete electric circuitry of the SWG is shown on Fig. 1, and the time-diagrams at certain concrete points are given on Fig. 2.

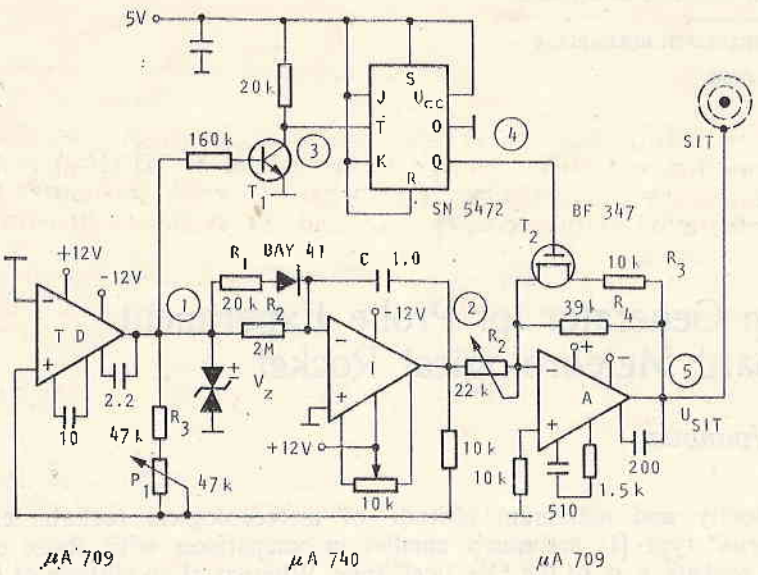

Fig. 1. The complete electric circuitry of the SWG

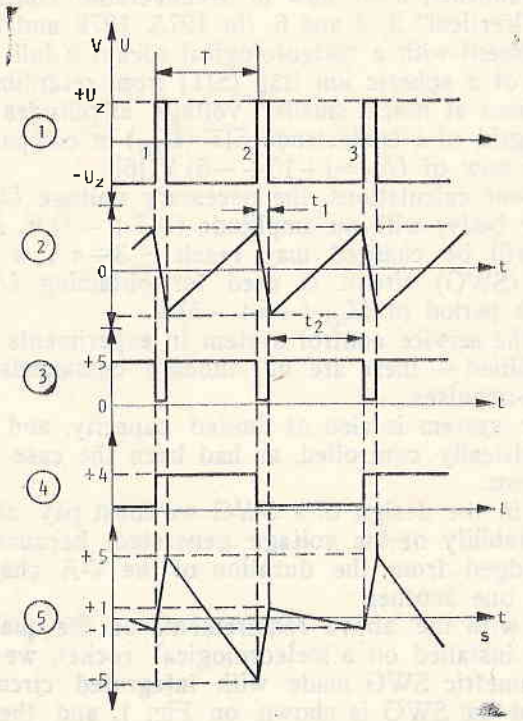

Fig. 2. The time diagrams at concrete points

The first step of the SWG is a threshold detector TD (comparator), while the second one is integrator I — both of them with operational amplifiers μA 709 and μA 740. The voltage at the output of TD (point 1) switches from $-U_z$ to $+U_z$ when the linearly increasing voltage at the output of I (point 2) becomes sufficiently positive so that the point A voltage rises above zero. The symmetrical and stable voltage at the output of TD (U_{TD}) is maintained by two equal Zener diodes oppositely connected, which guarantees the precision of integration of the voltages $\pm U_z$ and the symmetry of both threshold levels of switching.

The U_{TD} voltage is switched from $+U_z$ to $-U_z$ when the much more rapidly decreasing (linearly) voltage from the output of I (U_I) during the reverse run of the SWG (t_1) becomes sufficiently high so that the voltage at point A goes below zero.

The value of the potentiometer for the adjustment of the frequency of U_{SIT} is selected in such a way that the necessary period $T=1$ s shall be within the limits of ± 0.3 s.

The change of U_I in the positive direction (direct run t_2) is much longer in time, compared with t_1, because the time constant of the capacitor C in the feedback of I changes with the change of polarity of U_{TD} ($\pm U_z$). When $U_{TD}=+U_z$, C discharges mainly through the resistor R_1 and a diode in series, and the time constant R_1C is much smaller when $R_1 \ll R_2$. When $U_{TD}=-U_z$ the capacitor C is charged through R_2 much more slowly with a time constant R_2C. The values of R_1 and of R_2 are selected in such a way that at fixed levels $\pm U_z$ the reverse run shall be 1% of the direct one (in this case $t_1 \ll 10$ ms).

The transistor T_1 (buffer, invertor and limiter) forms the necessary voltage (point 3) for the command of the trigger J-K (logical integrated circuit SN 5472) according to clock input.

One of the outputs of the trigger (Q) feeds voltage (point 4) for the command of the key of a field transistor (FET-BF 347), connected in the feedback circuit of the inverting amplifier (A) of the voltage from I. In this way over one period the resistor R_3 is connected parallel to R_4 and the coefficient of amplification of A decreases five times (point 5) according to the requirements for the amplitude, as mentioned in the beginning.

The adjustment and fine tuning of the amplitude of the voltage U_{SIT} is done with the potentiometer P_2.

The circuit has been designed at the Central Laboratory for Space Research of the Bulgarian Academy of Sciences and the tests carried out with it demonstrated stable operation in a wide range of temperatures.

References

1. Viekran, Barabhai. Sounding Rockets Program "Centaure". Space Center ISRO, Trivandrum,
2. Serafimov, K. B., S. K. Chapkunov, M. Ch. Petrounova, T. N. Ivanova. — Space Research, XVII, 1977, 461-463.
3. Chapkunov, S., G. Gdalevich, M. Petrounova, T. Ivanova, L. Bankov. — Space Research, XVII, 1977, 457-459.
4. Chapkunov, S. K. — C. R. Acad. bulg. sci., 26, 1973, 8, 1033-1036.
5. Chapkunov, S. K., T. N. Ivanova, M. H. Petrounova, Z. I. Tzvetkov. — C. R. Acad. bulg. sci., 30, 1977, 3, 375-378.
6. Ivanova, T. N. — C. R. Acad. bulg. sci., 27, 1974, 12. 1663-1665.

Генератор развертки для зондового эксперимента на метеорологической ракете

Т. Иванова

(Резюме)

Зондовый метод исследования плазмы с помощью сферической ионной ловушки широко применяется при прямых космических измерениях. В сообщении коротко рассмотрены особенности эксперимента на метеорологической ракете в сравнении с использованными до сих пор для ионосферных измерений с болгарской зондовой аппаратурой геофизическими ракетами „Вертикаль". Применяется триэлектродная ловушка, к внешней сетке которой приложено пилообразное напряжение для получения характеристики зондового тока. Представлена принципиальная схема примененного генератора пилообразного напряжения с переменной амплитудой, разработанная на основании поставленных специфическим экспериментом требований.

BULGARIAN ACADEMY OF SCIENCES

SPACE RESEARCH IN BULGARIA, 3

Sofia · 1980

A Solution of the Problem of Rotation of the Celestial Bodies*

T. R. Tilchev

1. Introduction

For explanation of the axial rotation of the celestial bodies several hypotheses are proposed. Shmidt [1] considers the direct rotation of the planets and of the Sun as a result of the falling meteoric particles upon them. Artemyev and Radzievskii [2] assume that the meteoric particles falling on the planet transfer their positive momentums only and turn it directly about its own axis. Recently it was discovered, however, that Venus has a retrograde rotation. The planet Uranus is also rotating retrogradely. Alfven considers the axial rotation of the celestial bodies as a result of the action of magnetic forces. These hypotheses are not satisfactory and the phenomenon is still a topical problem. In this paper a new explanation of this phenomenon is proposed.

2. Method and Results

We proceed from the following original experiment. A homogeneous sphere with radius r is circulating in an circumference with radius r_1 lying in a horizontal plane. The sphere can rotate freely about its own axis perpendicular to the plane of the circumference. The system has two degrees of freedom. Let us designate by Ω_1 the initial angular velocity of the circular motion of the sphere, by Ω_2 the angular velocity of its circular motion at the end of a certain interval of time ΔT and by ω the angular velocity of the proper axial rotation of the sphere. We observe that

1. At $\Omega_1=\Omega_2=$ const, i. e. at a uniform circular motion $\omega=0$; the sphere does not rotate about its own axis.

2. At $\Omega_1>\Omega_2$, i. e. at a decelerate circular motion $\omega>0$; the sphere obtains a *direct* axial rotation.

3. At $\Omega_1<\Omega_2$, i. e. at an accelerate circular motion $\omega<0$; the sphere obtains a *retrograde* axial rotation.

*For open discussion.

It is not difficult to see that the axial rotation of the sphere is caused by the action of the unequal forces of inertia of the particles of the sphere which appear at the change of the angular velocity of its circular motion. The value of the forces of inertia of the particles of the sphere depends on their distance to the centre of the circumference and on the difference $|\Omega_1 - \Omega_2|$.

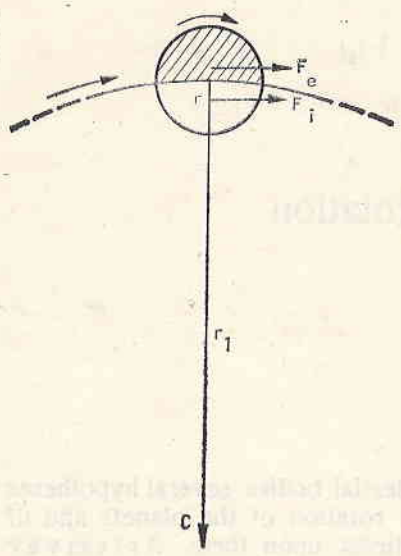

Fig. 1

The angular velocity of the circular motion of the sphere can be changed by direct action or by the change of the radius of the circumference from r_1 to r_2.

We have to determine the angular velocity of the axial rotation of the sphere ω obtained at the change of the angular velocity of its circular motion from Ω_1 to Ω_2.

We solve this problem in the following way. The cylindrical surface passing through the circumference and the rotational axis of the sphere divides the sphere in two parts: external one with mass m_1 and internal one with mass m_2, as shown in Fig. 1. We solve the problem at $r_1 \gg r$ so that we could assume $m_1 - m_2 = m$. A similar case we have, for example, at a spherical artifical Earth's satellite. The part of its orbit limited by the satellite is almost a straight line.

We designate by F_e and F_i the resultants of the particles' forces of inertia of the external (dashed) and internal hemispheres. We assume with sufficient accuracy that at $r_1 \gg r$ the fulcrums of the resultants F_e and F_i are at a distance equal to $3/8\,r$ from the centre of the sphere. We designate the force, which turns the sphere about its axis (directly at $\Omega_1 > \Omega_2$, as shown in Fig. 1, and retrogradely at $\Omega_1 < \Omega_2$) by F.

Obviously

(1) $$F = F_e - F_i,$$

or

(2) $$F = m a_e - (-m a_i),$$

where a_e and a_i are the tangential accelerations of the mass-centres of the external and internal hemispheres.

At the change of the angular velocity of the circular motion of the sphere from Ω_1 to Ω_2 the linear speed of the mass-centre of the external hemisphere changes from V_{e1} to V_{e2}, and that of the internal hemisphere from V_{i1} to V_{i2}. At the same time the mass-centre of the external hemisphere, where the fulcrum of the force F is formally assumed, passes a path $S = S_{e2} - S_{e1}$. Multiplying both parts of (2) by ds and integrating in the above limits we obtain

(3) $$\int_{S_{e1}}^{S_{e2}} F\,ds = \left| -m\int_{V_{e1}}^{V_{e2}} v\,dv - \left(-m\int_{V_{i1}}^{V_{i2}} dv\right) \right| = \left| m\int_{V_{e1}}^{V_{e2}} dv - m\int_{V_{i1}}^{V_{i2}} dv \right|,$$

(4) $$A = \left| \left(\frac{mV_{e1}^2}{2} - \frac{mV_{e2}^2}{2}\right) - \left(\frac{mV_{i1}^2}{2} - \frac{mV_{i2}^2}{2}\right) \right|,$$

where A is the work of the force F in the path S.

The kinetic energy E of the obtained axial rotation of the sphere is equal to the work of the force F, i. e. $E=A$

$$E=\frac{2}{5}X\frac{2mr^2\omega^2}{2}, \tag{5}$$

where $2m$ is the mass of the sphere. From (4) and (5) we obtain

$$\frac{4r^2\omega^2}{5}=(V_{e1}^2-V_{e2}^2)-(V_{i1}^2-V_{i2}^2)\ ; \tag{6}$$

$$V_{ei}=\Omega_1(r_1+3/8r);\quad V_{e2}=\Omega_2(r_1+3/8r);$$

$$V_{i1}=\Omega_1(r_1-3/8r);\quad V_{i2}=\Omega_2(r_1-3/8r).$$

With the above values of V_{e1}, V_{e2}, V_{i1} and V_{i2} in (6) we obtain

$$\pm\omega=\sqrt{\frac{15r_1}{8r}\left|(\Omega_1^2-\Omega_2^2)\right|}. \tag{7}$$

If the change of the angular velocity of the circular motion of the sphere is performed by changing the radius of the circumference from r_1 to r_2, formula (7) takes the form

$$\pm\omega=\sqrt{\frac{15}{8r}\left|(\Omega_1^2r_1-\Omega_2^2r_2)\right|}. \tag{8}$$

The relations (7) and (8) are valid in an uniform field of gravitation. For a homogeneous spherical satellite moving in a non-uniform field of gravitation, however, (4) has the form

$$A=E=\left|\left[\left(\frac{mV_{e1}^2}{2}+E_p^{e1}\right)-\left(\frac{mV_{e2}^2}{2}+E_p^{e2}\right)\right]-\left[\left(\frac{mV_{i1}^2}{2}+E_p^{i1}\right)-\left(\frac{mV_{i2}^2}{2}+E_p^{i2}\right)\right]\right|, \tag{9}$$

where E_p^e and E_p^i are the potential energies of the external and internal hemispheres of the satellite. At our laboratory experiment we have $E_p^{e1}=E_p^{e2}=E_p^{i1}=E_p^{i2}=mgh$, so that in this case (9) is reduced to (4).

The total energy of a homogeneous spherical Earth's satellite moving in a circular orbit is

$$E_k+E_p=\frac{GM2m}{2r_1}+GM2m\left(\frac{1}{R}-\frac{1}{r_1}\right)=CM2m\left(\frac{1}{R}-\frac{1}{2r_1}\right),$$

where M is the mass of the Earth, R is the average radius of the Earth, r_1 is the distance of the satellite to the centre of the Earth. For such a satellite passing from one orbit to another one (9) takes the form

$$\frac{2mr^2\omega^2}{5}=GMm\left|\left\{\left[\left(\frac{1}{R}-\frac{1}{2(r_1+3/8r)}\right)-\left(\frac{1}{R}-\frac{1}{2(r_2+3/8r)}\right)\right]\right.\right.$$

$$\left.\left.-\left[\left(\frac{1}{R}-\frac{1}{2(r_1-3/8r)}\right)-\left(\frac{1}{R}-\frac{1}{2(r_2-3/8r)}\right)\right]\right\}\right|. \tag{10}$$

From (10) we obtain

$$\pm\omega=\sqrt{\frac{15}{16r}\left|\left(\frac{GM}{r_1^2-(3/8r)^2}-\frac{GM}{r_2^2-(3/8r)^2}\right)\right|}. \tag{11}$$

The total energy of a homogeneous spherical Earth's Satellite moving in an eliptical orbit is

$$E_k+E_p=-GM2m\left(\frac{2}{r_1}-\frac{1}{a}\right)+GM2m\left(\frac{1}{R}-\frac{1}{r_1}\right)=GM2m\left(\frac{1}{R}-\frac{1}{2a}\right),$$

where a is the major semi-axis of the satellite's orbit. In this case we obtain from (9) in a similar way the following relation:

$$\pm\omega=\sqrt{\frac{15}{16r}\left|\left(\frac{GM}{a_1^2-(3/8r)^2}-\frac{GM}{a_2^2-(3/8r)^2}\right)\right|}. \tag{12}$$

At the movement of the the satellite in one orbit only we should have $a_1=a_2=\text{const}$, $E_k+E_p=\text{const}$ and $\omega=0$, i.e. in such a case the axial rotation of the satellite does not depend on its orbital motion.

For a homogeneous cylindrical satellite with moment of inertia $I=2m\left(\frac{r^2}{3}+\frac{z^2}{4}\right)$, we obtain the following relation

$$\pm\omega=\sqrt{\frac{r}{2\left(\frac{r^2}{3}+\frac{z^2}{4}\right)}\left|\left(\frac{GM}{a_1^2-(1/2r)^2}-\frac{GM}{a_2^2-(1/2r)^2}\right)\right|}, \tag{13}$$

where r is the rotational radius of the satellite equal to $H/2$, z is the radius of its cross-section. Passing from one orbit to another the satellite turns as an aircraft propeller, in the plane of its orbit. (We neglect the precession.)

The formulae (11), (12) and (13) give the angular velocity of a non-stabilized satellite if in the first orbit $\omega=0$. If in the first (initial) orbit $\omega>0$ or $\omega<0$, formulae (12), and (11) and (13) as well, should be written as follows:

$$\pm\Delta\omega=\sqrt{\frac{15}{16r}\left|\left(\frac{GM}{a_1^2-(3/8r)^2}-\frac{GM}{a_2^2-(3/8r)^2}\right)\right|}, \tag{12a}$$

where $\Delta\omega$ is the increment (positive or negative) of the angular velocity of the axial rotation of the satellite during a certain interval of time ΔT, during which a_1 changes to a_2.

As $a^2\gg(3/8r)^2$, formulae (12), and (11) and (12a) as well can be written in this form

$$\pm\omega=\sqrt{\frac{15}{16r}\left|\left(\frac{GM}{a_1^2}-\frac{GM}{a_2^2}\right)\right|}. \tag{14}$$

It is known that the light pressure provokes an essential perturbation of the orbit of the light spherical satellites at a height >700 km. By such a satellite we could verify formula (14). Determining the major semi-axis of its orbit in the beginning and in the end of a certain interval of time ΔT, we calculate ω by formula (14) and compare the result with the increment of ω during the same interval ΔT obtained by formula (15)

$$\pm\Delta\omega=|\omega_1-\omega_2|, \tag{15}$$

where ω_1 and ω_2 are the observed angular velocities of the axial rotation of the satellite in the beginning and in the end of the same interval ΔT. The results obtained could be verified by a special satellite launched for this purpose if it is possible to change the major semi-axis of its orbit in desired values.

The relations (7) and (8) could be verified under laboratory conditions.

A synchronous change of the orbital period and the period of the axial rotation of the second Soviet satellite (1957β) and the last stage of the third Soviet satellite (1958δ_1) with the change of the solar activity has been really

established [3]. The observed increase of the rotational period about the centre of mass of the last stage of the third Soviet satellite during its spiral approach to the Earth (from 8 to 9.5 s) [4] can be also explained by relation (13). The atmospheric resistance is believed to play a secondary role here. This factor is negligible for the massive satellites moving in the upper atmosphere.

At the verification of the relations obtained we must have in mind that the vector of the last push of the rocket does not always pass through the centre of mass of the satellite and would turn it about that centre [5]. Consequently, we must take the initial conditions into account.

The calculations by formula (12) show that a homogeneous spherical satellite, e. g. with radius $r=8$ m, passing from one orbit with major semi-axis $a_1=6{,}500$ km to a higher one with $a_2=6{,}650$ km, at initial condition $\omega=0$, turns directly about its centre of mass with angular velocity $+\omega=0.222$ rad/s, or with a period $t=28$ seconds. The same result but with retrograde rotation ($-\omega=0.222$ rad/s) should be obtained if this satellite passes from the higher to the lower orbit.

It is known that the equations of the passive flight of the artificial cosmic objects do not, as a matter of principle, differ from the equations of the motion of the natural celestial bodies. For this reason we could say that the relation (12) should be valid for the celestial bodies as well. The difference will be only in the corrections depending on the corresponding moment of inertia and the inclination of the rotational axis of the body to the plane of its orbit.

In rigid body dynamics it is assumed that the rotational motion of spherical and homogeneous bodies does not depend on their advance motion. The differential equations of the translatory motion and that of the rotational motion of the body about its centre of mass are considered separately. This statement is true, as we have seen, at rectilinear motion and at uniform circular motion of the body. It is not true at non-uniform circular or curvilinear motion of the body. The different forces of inertia of the particles of the body which appear in such a case have not been taken into account.

An important role for the difficulties arising at the solution of the problem of the axial rotation of the celestial bodies is played by the theorem of Lagrange-Laplace for the stability of the solar system. We have seen that at $a=$ const the axial rotation of the satellite does not really depend on its orbital motion. The investigations of the series which are used in celestial mechanics in the theory of perturbations show, however, that they are divergent as a rule. The theorem of Lagrange-Laplace is not strictly proved. A. Friedman has proved that the Universe is periodically expanding and contracting [7]. The expansion of the Universe was confirmed by observation (Hubble's law). According to R. Zaikov the Sun has orbital acceleration [8, 9]. The inner satellite of the planet Mars, Phobos, also has orbital acceleration [6]. Consequently, the solar system is not stable during long periods of time lasting millions and billions of years.

According to the hypothesis of V. G. Fessenkov the planets of the solar system had been formed far nearer to the Sun, in comparison with their present distance. Consequently, during the first period of their existence the planets had been moving off in spirals from the Sun, and according to relation (12) they obtained their direct axial rotation. The observed retrograde rotation of the planet Venus could be explained with the same relation (12) if this planet has orbital acceleration. According to N. Bonev the young planet should have a retrograde axial rotation thanks to the Keplerian distribution of the velocities of its particles [9]. Such an explanation of the retrograde rotation of

Venus does not contradict our theory. According to (12), at the moving off from the Sun the unequal forces of inertia of the perticles of the planet could brake the retrograde rotation of the planet and turn it directly in the course of time. During the second period of existence of the planet, when it approaches the Sun, the forces of inertia which are acting in the opposite direction could brake the direct rotation of the planet and turn it retrogradely. It is necessary to know how the major semi-axis of the orbit of Venus is changing. This will show us whether Venus is a young or old planet.

The transition of the direct axial rotation of the celestial body to a retrograde rotation is probably achieved simultaneously with the change of the inclination of its rotational axis to the normal to its orbit plane. At an inclination of $>90°$ the direct rotation turns to retrograde. The inclination of the planet Uranus, which is rotating retrogradly, is 98°. The inclination of Venus is $\approx 90°$ (probably $>90°$). The Moon is in a state of gravitational stabilisation.

Formula (12) or (14) make it possible to determine approximately at what distance from the Sun the planets had been formed. For our Earth, for example, at $M=2\times10^{33}$ g (the mass of the Sun), $a_2=1.496\times10^{13}$ cm, $\omega=7.292\times10^{-5}$ rad/s, formula (14) gives $a_1=56$ millions of kilometres. This result is in a very good agreement with Fessenkov's hypothesis.

The orginal experiment with the homogeneous sphere giving a qualitative explanation of the axial rotation of the celestial bodies, which is the base for our investigation of this phenomenon, was performed by the author's father Rasho Tilchev in 1932.

Acknowledgement. I am very grateful to the staff of the Central Laboratory for Space Research of the Bulgarian Academy of Sciences for the kind support in publishing my paper.

References

1. Шмидт, О. Ю. Избранные труды, геофизика и космогония. — АН СССР. М., 1960.
2. Артемьев, А. В., В. В. Радзиевски. О происхождении осевого вращения планет.— Астрономический журнал, Том XVII, Вып. I. М., 1965.
3. Григоревский, В. М. О связи периода вращения спутника 1958 δ_1 с солнечной активностью. — В: Исскуственные спутники Земли, вып. 17. М., 1963, 82.
4. Кинг-Хили. Д. Исскусственные спутники и научные исследования. М., 1963.
5. Белицкий, Б. В., Ю. В. Зонов. Вращение и ориентация третьего советского спутника. — В: Искусственные спутники Земли, вып. 7. М., 1961, 32.
6. Демин, В. Г. Судьба Солнечной системы. М., 1969.
7. Тростников, В. Н. Дифференциальные уравнения в современной науке. М., 1966.
8. Зайков, Р. Г. О зависимости между обращением системы млечного пути и геологическими циклами. — Доклады БАН, 21, 6, 1968.
9. Зайков, Р. Г. Космологические основы абсолютной геохронологии. — Изв. секц. астрономия. Том I. С., 1970.
10. Бонев, Н. О ретроградной ротации Венеры (II). — Изв. секц. астрономия, Том I. С., 1970.

Решение проблемы о вращении небесных тел

Т. Р. Тилчев

(Резюме)

В этой статье дается теоретическое объяснение экспериментально установленной зависимости между неравномерным круговым поступательным движением однородной сферы и ее собственным осевым вращением. На основании полученной зависимости предлагается оригинальное решение проблемы осевого вращения небесных тел и неориентированных спутников Земли.